BRNO UNIVERSITY OF TECHNOLOGY

VYSOKÉ UČENÍ TECHNICKÉ V BRNĚ

FACULTY OF MECHANICAL ENGINEERING

FAKULTA STROJNÍHO INŽENÝRSTVÍ

INSTITUTE OF PHYSICAL ENGINEERING

ÚSTAV FYZIKÁLNÍHO INŽENÝRSTVÍ

DEVELOPMENT OF THE SCANNING TIME-RESOLVED KERR MICROSCOPE

VÝVOJ KERROVA MIKROSKOPU S ČASOVÝM ROZLIŠENÍM

BACHELOR'S THESIS

BAKALÁŘSKÁ PRÁCE

AUTHOR — **Zdeněk Nekula**

AUTOR PRÁCE

SUPERVISOR — **Ing. Ondřej Wojewoda**

VEDOUCÍ PRÁCE

BRNO 2021

BRNO UNIVERSITY OF TECHNOLOGY
FACULTY OF MECHANICAL ENGINEERING

Assignment Bachelor's Thesis

Institut:	Institute of Physical Engineering
Student:	**Zdeněk Nekula**
Degree programm:	Applied Sciences in Engineering
Branch:	Physical Engineering and Nanotechnology
Supervisor:	**Ing. Ondřej Wojewoda**
Academic year:	2020/21

As provided for by the Act No. 111/98 Coll. on higher education institutions and the BUT Study and Examination Regulations, the director of the Institute hereby assigns the following topic of Bachelor's Thesis:

Development of the scanning time–resolved Kerr microscope

Brief Description:

Nowadays, the CMOS technology is reaching its fundamental limits. There is a need to search for new innovative approaches, which will be more efficient and faster. One of the most promising candidates is the approach exploiting phenomena connected with magnetization dynamics. To be able to design devices based on these phenomena we need tools capable to probe magnetization on the femtosecond timescale. One of the techniques, which can be used for this purpose is time–resolved Kerr microscopy. The goal of the bachelor thesis is to develop time–resolved scanning Kerr microscope (TR–SKM) and test its functionality on a series of experiments.

Bachelor's Thesis goals:

Perform literature search and describe current state of the art of Kerr microscopy with emphasize to time–resolved measurements.
Build and characterize a setup for TR–Kerr measurement.
Prove the functionality of the setup with series of experiments.

Recommended bibliography:

MCCORD, Jeffrey, 2015. Progress in magnetic domain observation by advanced magneto-optical microscopy. Journal of Physics D: Applied Physics. 48(33), 1-43. ISSN 0022-3727. Dostupné z: doi:10.1088/0022-3727/48/33/333001

STIGLOHER, Johannes, 2018. Reflection and Refraction of Spin Waves. Regensburg.
Doktroská teze. Universität Regensburg. Vedoucí práce Prof. Dr. Christian Back.

Deadline for submission Bachelor's Thesis is given by the Schedule of the Academic year 2020/21

In Brno,

L. S.

prof. RNDr. Tomáš Šikola, CSc.	doc. Ing. Jaroslav Katolický, Ph.D.
Director of the Institute	FME dean

Abstract

In recent days, magnetic materials, structures, and devices are getting more popular, especially those related to spintronics. Research and development of such magnetic samples require a way to observe magnetization with good spatial and temporal resolution. Most dynamic changes of magnetization are realized in nanoseconds or even faster. If we can detect these dynamic processes, we can reveal many exciting magnetization features and add the fourth dimension to our experiments. We introduce a scanning Kerr microscope working in two modes: static and dynamic. In static mode, our microscope detects a direction of magnetization in a variable magnetic field. In dynamic mode, we use a pump-probe method to reach a temporal resolution and observe a fast evolution of magnetization.

Abstrakt

V těchto dnech jsou magnetické materiály, struktury a zařízení stále více populární. Především ty, které souvisejí se spintronikou. Výzkum a vývoj takových magnetických vzorků vyžaduje způsob pozorování magnetizace s dobrým prostorovým i časovým rozlišením. Mnoho dynamických změn magnetizace probíhá v řádech nanosekund, nebo ještě rychleji. Pokud můžeme detekovat tyto dynamické procesy, tak můžeme odhalit mnoho zajímavých magnetických vlastností a obohatit naše experimenty o čtvrtou dimenzi. Představujeme skenovací Kerrův mikroskop pracující ve dvou režimech: statickém a dynamickém. Ve statickám reřimu náš mikroskop detekuje směr magnetizace v proměnném magnetickém poli. V dynamickém režimu používáme pump-probe metodu k dosažení časového rozlišení a pozorování rychlého vývoje magnetizace v čase.

Keywords

Kerr microscope, Kerr effect, time resolution, pump-probe, vortex.

Klíčová slova

Kerrův mikroskop, Kerrův jev, časové rozlišení, pump-probe, vortex.

NEKULA, Zdeněk. Development of the scanning time-resolved Kerr microscope. Brno, 2021. Bachelor's Thesis. Brno University of Technology. Faculty of Mechanical Engineering, Institute of Physical Engineering. Supervisor Ondřej Wojewoda.

I declare that I have written my bachelor's thesis on the theme of Development of the scanning time-resolved Kerr microscope independently, under the guidance of the supervisor Ondřej Wojewoda, and using the sources quoted in the list of literature at the end of the thesis.

Zdeněk Nekula

Acknowledgment

I am grateful to Ondřej Wojewoda, who introduced me to the CEITEC laboratories at the very beginning of my university studies. Later, he supervised my bachelor's work and corrected my thesis. I want to thank him for his time, all discussions, and wise advice.

My thanks also go to the whole research group of Nanomagnetism and spintronics at CEITEC. Especially to Michal Urbánek, who led the project of microscope Miranda 5.0. He was always interested in my activity in the laboratory and gave me so many interesting possibilities. Then, I am thankful to Lukáš Flajšman, who made the previous versions of the microscope, and I continue in his work. I want to mention Marek Vaňatka, who was always ready to help with any practical issue. I thanks also to Igor Turčan, who red my thesis and give me many suggestions. I want to point out also Libor Vojáček. It was great to cooperate with him at the optical table, and I am grateful that he allowed me to use his devices for pre-testing. I should also mention Dominik Varga, the best turner I know, who manufactured many components for the microscope Miranda. I am thankful to all the others in our group, in CEITEC, and also to the other students and professors in our university since they create such a good environment.

I am proud of my parents that they support me in making the right decisions.

I am very grateful to God. When I was finishing the optical setup of the microscope Miranda, I struggled to find a correct alignment for five months. I was depressed in my useless work at that time. One morning, I told God that I want to cooperate with him in research, and I am giving him this work. I promised him to write an acknowledgment in my thesis if the microscope would work. The same day in the evening, I finally succeed. I found the correct alignment and started to measure valuable data. „Thank you, God, you are great!“

Zdeněk Nekula

CzechNanoLab project LM2018110 funded by MEYS CR is gratefully acknowledged for the financial support of the measurements/sample fabrication at CEITEC Nano Research Infrastructure.

Contents

Introduction 1
1 Electromagnetic Waves 2
1.1 Maxwell Equations 2
1.2 Polarization 4
1.3 Jones Formalism 4
1.4 Rotation and Ellipticity 7
2 Kerr Effect 9
2.1 Magnetization and Kerr Effect 9
2.2 How to Compute the Jones Reflection Matrix 10
2.2.1 Step 1: Input parameters 11
2.2.2 Step 2: Angles of Propagation and Wave numbers 12
2.2.3 Step 3: Boundary and Propagation Matrices 12
2.2.4 Step 4: T Matrix 14
2.2.5 Step 5: Jones Reflection Matrix 14
2.3 Voigt Vector and Permittivity Tensor 15
2.4 Numerical Calculations 16
3 Microscope – Optics and Analog Signal Processing 18
3.1 Kerr Microscopy 18
3.2 Miranda Microscope Overview 19
3.3 Laser Optics of Miranda 20
3.3.1 He-Ne Laser 20
3.3.2 Half-Wave Plate 21
3.3.3 Beam Expander 21
3.3.4 Mirrors 21
3.3.5 Linear Polarizer 21
3.3.6 Objective 22
3.3.7 Quarter Wave Plate 25
3.3.8 The Half Wave Plate 25
3.3.9 Wollaston Prism 25
3.3.10 Four-Quadrant Detectors 25
3.4 Camera Imagining 26
3.4.1 Single LED Source 26
3.4.2 Objective 26

3.4.3 High Pass Filter 26
3.4.4 Camera 26
3.5 Signal Processing in Miranda Microscope 26
3.5.1 Magnetic field 27
3.5.2 Amplifiers 27
4 Microscope - Mechanical Design 28
4.1 Sample Stage 31
4.2 Objectives 31
4.3 Electromagnet 32
5 Software and measurement 34
5.1 Thatec 34
5.2 Data processing 35
5.3 Experimental Results of the Scanning Mode 37
5.4 Experimental Results of the Rotation Mode 40
6 Time Resolution 42
6.1 Pump-Probe 42
6.2 Setup for the Time Resolution 43
6.3 Sample 44
6.4 Measurement 47
Conclusion 52
Bibliography 53
List of Abbrevitations 55

Introduction

In the last decades, we have seen the rapid progress of information technologies (IT). This was closely connected with magnetic materials used to store data. A known example is a floppy disc and later a hard drive. Current research aims to find new ways for future IT. Therefore, our laboratory focuses on the study of spin waves [1,2]. Spin waves are an interesting phenomenon with promising features, such as low excitation energy, that could be used in future logic operations [1,3–6].

Kerr microscope is an essential tool in magnetic research [7,8]. It offers data about the surface magnetization using only a light reflection on an inspected sample. Lukáš Flajšman started to build a Kerr microscope called Miranda approximately in 2012 [9][10][11]. We want to continue in his work and develop already the fifth version, the *Miranda 5.0*.

This scanning Kerr microscope can observe not only magnetic structures in an equilibrium state but also dynamic changes of magnetization. Miranda should become a tool for standard measurement with user-friendly software.

We made a 3D model of the microscope and ordered new components. We rebuild a whole construction and add a new electromagnet on rails. We also cooperated with Thatec to develop control software. Then, we aligned the optics and added dynamic measurement with time resolution.

The first and the second chapter are theoretical. The first one introduces a reader to optics, light polarization, and Jones formalism. The second one concerns the Kerr effect and related numerical calculations.

The following chapters describe our microscope Miranda, its optical system and mechanical design, signal processing, and software. We also show measurements at Miranda 5.0 and demonstrate what the microscope offers to any user.

1 Electromagnetic Waves

In this chapter, we focus on light, or more generally, electromagnetic waves. Light is a fundamental medium that can interact with a magnetic field, and we can use it to probe magnetized structures, which are the main object of our interest.

We will quickly introduce electromagnetic waves - their derivation from Maxwell equations and basic properties. Then, we will continue with polarization, especially with Jones formalism which we use to describe the polarization of a beam after passing any optical elements.

1.1 Maxwell Equations

The simplest form of an electromagnetic wave is a monochromatic plane wave derived from Maxwell equations:

$$\begin{aligned} \nabla \cdot \boldsymbol{E} &= \frac{1}{\epsilon_0}\,\rho \\ \nabla \cdot \boldsymbol{B} &= 0 \\ \nabla \times \boldsymbol{E} &= -\frac{\partial \boldsymbol{B}}{\partial t} \\ \nabla \times \boldsymbol{B} &= \mu_0 \boldsymbol{J} + \mu_0 \epsilon_0 \frac{\partial \boldsymbol{E}}{\partial t}\ . \end{aligned} \tag{1.1}$$

For further information about derivation, I recommend a textbook written by Griffiths: “Introduction to Electrodynamics” [12].

Following the approach described in [9], we obtain this set of equations:

$$\boldsymbol{E}(\boldsymbol{r},t) = \boldsymbol{E_0}\cos(\boldsymbol{k}\cdot\boldsymbol{r} - \omega t + \varphi) \tag{1.2}$$

$$\boldsymbol{B}(\boldsymbol{r},t) = \boldsymbol{B_0}\cos(\boldsymbol{k}\cdot\boldsymbol{r} - \omega t + \varphi). \tag{1.3}$$

We receive these two equations (1.2), (1.3) of a monochromatic plane wave imaged in Figure 1.1. Here $\boldsymbol{E}$ is electric intensity and $\boldsymbol{B}$ is magnetic induction, **r** is a position vector, $\boldsymbol{k}$ is wave vector in the direction of propagation, ω is an angular frequency, and φ is phase offset, $\boldsymbol{E_0}$ and $\boldsymbol{B_0}$ are vectors determining direction and amplitude. $\boldsymbol{E}$ and $\boldsymbol{B}$ are perpendicular to each other, and their magnitudes are related by equation (1.4), where v is (phase) velocity of light in a specific medium

$$E_0 = \frac{B_0}{v}. \tag{1.4}$$

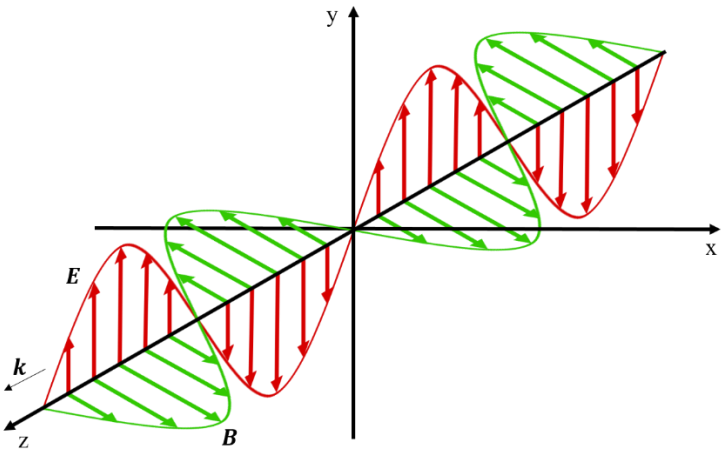

Figure 1.1: Electromagnetic wave propagating in the z-direction. Electric field **E** and magnetic induction B are perpendicular to each other, and vector k is pointing in the direction of propagation.

This relationship allows us to consider only one of these quantities since the second can usually be quickly related. In further consideration, we choose electric field $\boldsymbol{E}$ because of its more substantial impact on charged particles and matter.

An electric field's temporal and spatial shape (1.2) is one nonending sinusoidal (harmonic) plane wave. This means that it oscillates at one particular frequency:

$$f = \frac{\omega}{2\pi}.$$

For easier handling, we rewrite equations (1.2) and (1.3) into a complex form:

$$\widetilde{\boldsymbol{E}}(\boldsymbol{r},t) = \widetilde{\boldsymbol{E}}_{\boldsymbol{0}}\, e^{i(\boldsymbol{k}\cdot\boldsymbol{r}-\omega t)} \tag{1.5}$$

$$\widetilde{\boldsymbol{B}}(\boldsymbol{r},t) = \widetilde{\boldsymbol{B}}_{\boldsymbol{0}}\, e^{i(\boldsymbol{k}\cdot\boldsymbol{r}-\omega t)}, \tag{1.6}$$

where $\widetilde{\boldsymbol{E}}$, $\widetilde{\boldsymbol{B}}$ are complex electric intensity and magnetic induction, respectively. The real parts of $\widetilde{\boldsymbol{E}}$, $\widetilde{\boldsymbol{B}}$ are electric intensity and magnetic field with physical significance:

$$\boldsymbol{E} = Re\left(\widetilde{\boldsymbol{E}}(\boldsymbol{r},t)\right)$$

$$\boldsymbol{B} = Re\left(\widetilde{\boldsymbol{B}}(\boldsymbol{r},t)\right).$$

Here, the phase shift φ is included in complex amplitude $\widetilde{\boldsymbol{E}}_{\boldsymbol{0}}$, and $\widetilde{\boldsymbol{B}}_{\boldsymbol{0}}$.

In complex notation, we can also write an alternative to equation (1.4)

$$\widetilde{\boldsymbol{B}}(\boldsymbol{r},t) = \frac{1}{v}\widehat{\boldsymbol{k}} \times \widetilde{\boldsymbol{E}}(\boldsymbol{r},t) \tag{1.7}$$

Where $\widehat{\boldsymbol{k}}$ is a real unit vector pointing in the direction of wave propagation, and v is the speed of light.

1.2 Polarization

This section explains what polarized and unpolarized light is. If we take one monochromatic electromagnetic wave as described by (1.2), we see that the vector of electric intensity $\boldsymbol{E}$ oscillates in the direction $\boldsymbol{E_0}$. Vectors $\boldsymbol{E}$ and $\boldsymbol{k}$ are both in one plane, which is called the plane of polarization. Vector $\boldsymbol{B}$ is normal to this plane. Such light is linearly polarized.

Another case of polarization is circular polarization. Here, electric intensity rotates either clockwise or counterclockwise. Circularly polarized waves can be made by adding two identical linearly polarized waves but with mutually perpendicular polarization planes and phase shift $\varphi = \pi/2$.

Linear and circular polarization are just particular cases of general elliptical polarization. Any elliptical polarization can be made by adding two linearly polarized waves with mutually perpendicular polarization planes, but each with any magnitude and phase shift.

All cases mentioned above are called polarized. If we want to compose unpolarized light, we must add many electromagnetic waves of random polarization and random phase shifts. In this case, a static observer is exposed to light whose direction of polarization is changing so rapidly and randomly that we can call it generally unpolarized [13].

In this work, we focus on the case of polarized light. In the following text, we depict formalism for the description of the polarization state of the light.

Lightwave can be decomposed into two independent orthogonal modes. This means it is possible to find such pairs of electromagnetic waves that can, in combination, compose any polarization. We call them basis.

One of the possible bases consists of two perpendicularly polarized waves. If the propagation is along the z-axis in cartesian coordinates, then one is polarized in x and another in the y-direction. Another basis can be made from two circularly polarized waves, one clockwise and the other one counterclockwise.

The linearly polarized basis is used in Jones Formalism, useful for describing polarization of light beam as it goes through complex optical systems. Nevertheless, if one wants to describe partially polarized light, which is a combination of polarized and unpolarized light, it is necessary to use different formalism, for example, Poincare sphere.

1.3 Jones Formalism

We explain Jones formalism that we later use to describe the behavior of light as it goes through the developed microscope. In this section, the explanation follows the master thesis of Lukáš Flajšman [9].

As mentioned earlier, any polarized light can be composed of two linearly polarized electromagnetic waves. Here, if light propagates along the *z*-axis, we can talk about x-polarized or y-polarized light.

Light changes the direction of propagation in the case of reflection on a sample. We cannot find one Cartesian coordinate system, where the beam propagates along the *z*-axis before and after reflection. Therefore, it is better to use a system that is directly connected with propagating light. We define three normal axes: the first (***k***) pointing in the direction of propagation, the second (***s***) perpendicular to the plane of incidence, and the third (***p***) parallel to the plane of incidence. In the same way, we define *s* and *p* polarized light. These two letters are abbreviations of German words *senkrecht* (perpendicular) and *parallel* (parallel). As shown in Figure 1.2, *s*-polarization is perpendicular to the plane of incidence, and *p*-polarization is parallel to the plane of incidence.

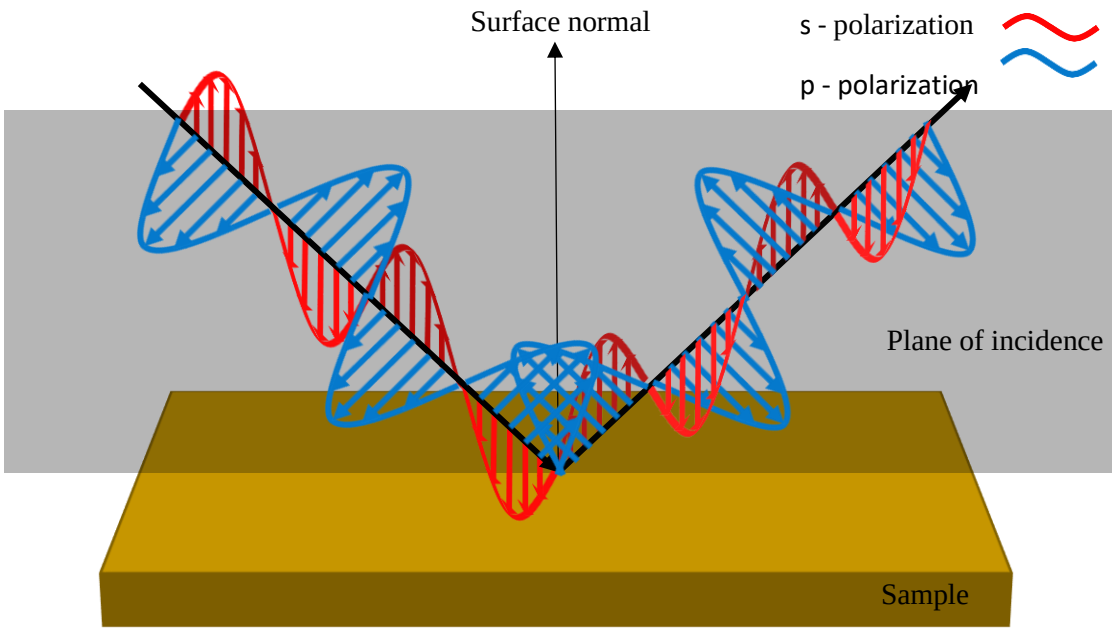

Figure 1.2:Sketch of the s-polarization and p-polarization in reflection on a sample

In Jones formalism, the state of the polarized beam at a certain position of beam path is fully described by complex Jones vector ***J*** that contains electric fields in *s* and *p* direction according to (1.5)

$$\boldsymbol{J}(t) = \begin{bmatrix} \tilde{E}_s \\ \tilde{E}_p \end{bmatrix} = e^{i\omega t} \begin{bmatrix} E_{s\,\max} & e^{i\varphi_s} \\ E_{p\,\max} & e^{i\varphi_p} \end{bmatrix}. \tag{1.8}$$

The first member on the right side ($e^{i\omega t}$) is a temporal factor. It is usually omitted because the frequency of light is relatively high ($f = \omega/2\pi$), and usually, we measure only the time-average of the intensity. For simplicity, we set the time *t* equal to zero:

$$\boldsymbol{J} = \begin{bmatrix} \tilde{E}_s \\ \tilde{E}_p \end{bmatrix} = \begin{bmatrix} E_{s\,\max}\ e^{i\varphi_s} \\ E_{p\,\max}\ e^{i\varphi_p} \end{bmatrix} \tag{1.9}$$

Basic polarization states are given in the Table 1.1:

Table 1.1 Examples of fundamental polarizations in Jones notation.

s-polarization	$\boldsymbol{J} = \begin{bmatrix} 1 \\ 0 \end{bmatrix}$
p-polarization	$\boldsymbol{J} = \begin{bmatrix} 0 \\ 1 \end{bmatrix}$
right-hand circular polarization	$\boldsymbol{J} = \begin{bmatrix} 1 \\ i \end{bmatrix}$
left-hand circular polarization	$\boldsymbol{J} = \begin{bmatrix} 1 \\ -i \end{bmatrix}$

Two following equations (1.10) and (1.11) defines light intensity *I* – optical power per unit area. The light intensity is what we measure, and therefore it is necessary to know its relation to electric intensity ***E***:

$$I = \frac{1}{2} c\, e_0\, E_0^2 \tag{1.10}$$

$$I = \frac{1}{2} c\, e_0\ \ \boldsymbol{J}^{\dagger} \cdot \boldsymbol{J}\,. \tag{1.11}$$

Here, † means a Hermitian adjoint (complex conjugate) of the vector.

In any optical setup, a light beam changes as it passes through (or reflects on) optical elements. Optical elements can be represented by 2×2 matrix operators $\hat{\boldsymbol{J}}$ acting on Jones vectors. Let us show critical Jones operators in the following Table 1.2.

Table 1.2 Jones operators of essential optical elements.

Horizontal polarizer	$\hat{\boldsymbol{J}}_{\mathrm{HP}}$	$\begin{bmatrix} 1 & 0 \\ 0 & 0 \end{bmatrix}$
Vertical polarizer	$\hat{\boldsymbol{J}}_{\mathrm{VP}}$	$\begin{bmatrix} 0 & 0 \\ 0 & 1 \end{bmatrix}$
Rotation of coordinates	$\hat{\boldsymbol{J}}_{ROT}\,(\alpha)$	$\begin{bmatrix} \cos\alpha & \sin\alpha \\ -\sin\alpha & \cos\alpha \end{bmatrix}$
General polarizer	$\hat{\boldsymbol{J}}_{\mathrm{P}}\,(\alpha) = \hat{\boldsymbol{J}}_{\mathrm{ROT}}(-\alpha)\ \hat{\boldsymbol{J}}_{\mathrm{HP}}\ \hat{\boldsymbol{J}}_{\mathrm{ROT}}(\alpha)$	$\begin{bmatrix} \cos^2\alpha & \cos\alpha\sin\alpha \\ \cos\alpha\sin\alpha & \sin^2\alpha \end{bmatrix}$

Gray filter	$\hat{\boldsymbol{J}}_{\mathrm{F}}(t)$	$\begin{bmatrix}\sqrt{t} & 0\\ 0 & \sqrt{t}\end{bmatrix}$
Dichroic retarder	$\hat{\boldsymbol{J}}_{\lambda}(\delta)$	$\begin{bmatrix}e^{i\delta} & 0\\ 0 & 1\end{bmatrix}$
Quarter-Wave plate $\left(\delta=\frac{\pi}{2}\right)$	$\hat{\boldsymbol{J}}_{\mathrm{QWP}}$	$\begin{bmatrix}e^{i\pi/2} & 0\\ 0 & 1\end{bmatrix}$
Half-Wave plate $(\delta=\pi)$	$\hat{\boldsymbol{J}}_{\mathrm{HWP}}$	$\begin{bmatrix}1 & 0\\ 0 & -1\end{bmatrix}$
Wollaston prism	$\hat{\boldsymbol{J}}_{\mathrm{W}}$	$\begin{bmatrix}1 & 0\\ 0 & 0\end{bmatrix}$; $\begin{bmatrix}0 & 0\\ 0 & 1\end{bmatrix}$

The scope of this thesis is not to elaborate on each element. One note to the gray filter, here variable *t* means decrement of intensity. If *t* = ½, then the light intensity we defined in equation (1.11) decreases to half.

$$I_f = t\, I_i$$

Usually, some components need to be rotated to have the desired properties. To do so in Jones formalism, we rotate the coordinate system by $\hat{\boldsymbol{J}}_{ROT}$ there and back as shown in a general polarizer, which is nothing else than horizontal polarizer rotated over angle α.

In case we want to serially combine several optical elements, in Jones formalism, we just let appropriate operators act on the initial (source) Jones vector $\boldsymbol{J}_i$ in the correct order,

$$\boldsymbol{J}_f = \hat{\boldsymbol{J}}_n \dots \hat{\boldsymbol{J}}_3 \hat{\boldsymbol{J}}_2 \hat{\boldsymbol{J}}_1 \;\; \boldsymbol{J}_i. \tag{1.12}$$

Here $\boldsymbol{J}_f$ is a final Jones vector after passing all n optical elements.

1.4 Rotation and Ellipticity

Usually, if we measure a polarized light, we are interested in two fundamental values: rotation and ellipticity. Their meaning is visible in polarization patterns (the pattern drawn by a vector $\boldsymbol{E}$ during one period – see Figure 1.3).

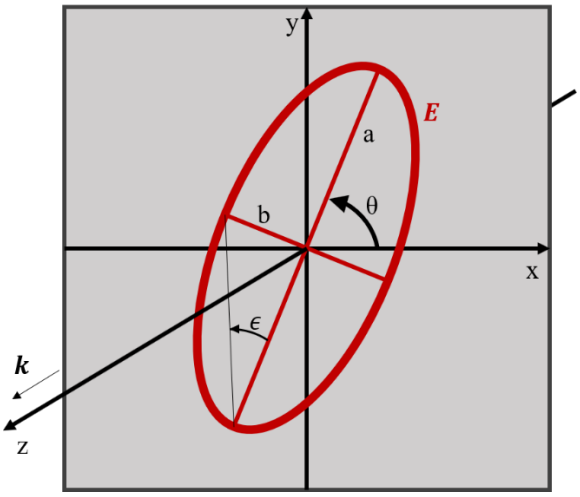

Figure 1.3: Polarization pattern containing rotation (azimuth angle) θ, ellipticity e and ellipticity angle ϵ.

Rotation (azimuth) θ is an angle between the x-axis (or s axis) and the major axis of the elliptical pattern

$$\theta \in \langle -\pi/2; \pi/2 \rangle$$

Ellipticity e is the ratio of minor axis (b) and major axis (a). Ellipticity angle ϵ is defined as arcus tangent of ellipticity:

$$e = \pm\frac{b}{a} = \tan(\epsilon) \tag{1.13}$$

According to the convention, the sign of the ellipticity is chosen: in this thesis, we will use plus for right-handed and minus for left-handed polarization.

At the moment, foundations of electromagnetic waves are built, and we have introduced the Jones formalism, which is an efficient tool to describe any state of polarized light.

2 Kerr Effect

We come to the core topic of this theoretical part, which is the magneto-optical Kerr effect. The magneto-optical Kerr effect is a change of polarization of light while reflecting on a magnetized media. First, we introduce basic terms connected to magnetization. Then, we present the Kerr effect itself, and at the end, a numerical tool for calculating the Jones reflection matrix which represents the polarization changes.

2.1 Magnetization and Kerr Effect

In the magnetized layer, the magnetization vector can be directed in three basic directions:

Longitudinal – parallel to the surface, in the plane of incidence.

Transversal – parallel to the surface, normal to the plane of incidence.

Polar – normal to the surface.

Now, we can imagine a metal layer. Here on the top surface, a laser beam is reflected at an angle α_i as pictured in Figure 3.1. The light gets several nanometers into the sample, and we can say that it travels some trajectory there and back. This means that reflection does not perform only on the first top atomic layer but spreads as deep as the light can penetrate. Since the amplitude of electromagnetic waves in metals drops exponentially, we can consider only short penetration depth, where the intensity is not negligible. It is several tens of nanometers. We recommend looking at experimental results of penetration depth in [14].

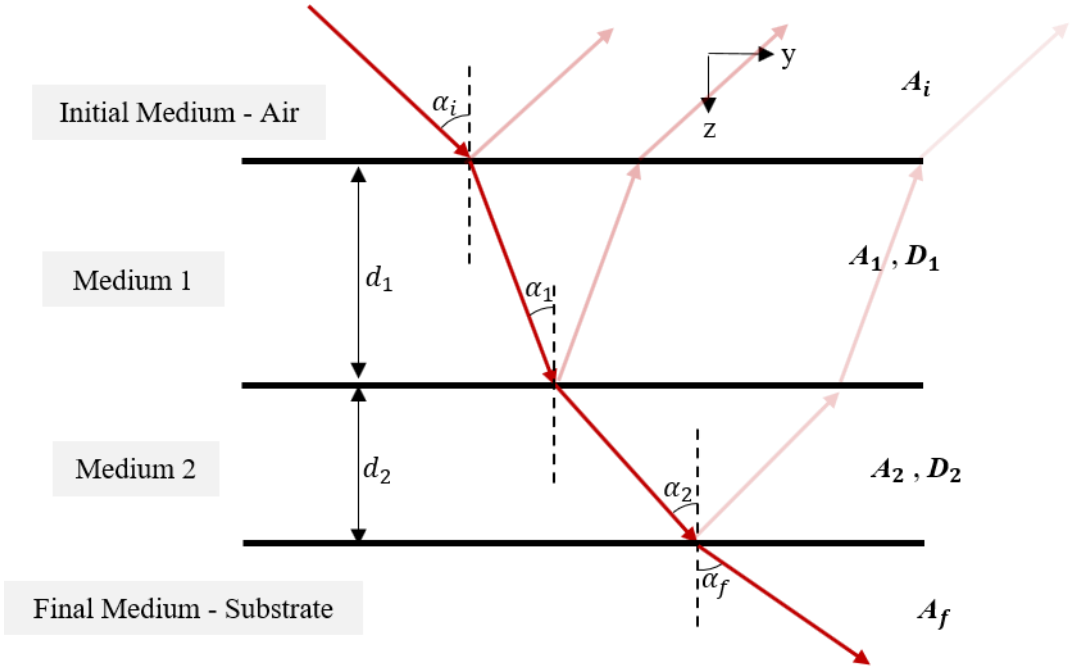

Figure 2.1 Beam reflection at a sample consisting of two layers on a substrate. A_m and D_m are m-th medium boundary matrix and propagation matrix, respectively (see Figure 2.2).

Both ellipticity and rotation can be altered during reflection. These changes can be caused either by a specific anisotropy of the media [15] or by a magnetic field. The magnetic field must be very strong to cause measurable changes in such a short trajectory. So strong field appears in magnetized materials, for example, in permalloy [16]:

$$B_s = \mu_0 M_s \approx 1 \text{ Tesla.}$$

Here B_s is the magnetic field of a saturated medium, μ_0 vacuum permeability, M_s saturated magnetization[1].

The polarization changes that are induced by a magnetic field are the Kerr effect.

As explained in [14], we can consider a light beam as a combination of a left-handed circular polarized (LCP) wave and a right-handed circular polarized (RCP) wave. If an RCP wave penetrates through a matter, surrounding electrons also perform slight right-handed circular motion (left-handed circular motion in the case of LCP wave). For example, the applied magnetic field in the positive *y*-direction, according to Figure 2.2, acts by Lorenz force to the rotating electrons. Right-handed circular trajectories will be enlarged and left-handed suppressed. We see that LCP and RCP waves are no longer equivalent, and the stronger the magnetic field, the more significant difference.

We do not want to derive exact equations based on this simplified model of circling electrons. Still, we can generally conclude that LCP and RCP waves can have different propagating speeds in a magnetized medium. This is expressed as a difference in real parts of refraction indexes, which causes rotation of the plane of polarization. LCP and RCP waves can also differ in damping. This is expressed as a difference in the imaginary part of the refraction index, which causes a change of ellipticity.

2.2 How to Compute the Jones Reflection Matrix

The following computing process was introduced in [14], and we draw it entirely in Figure 2.2.

[1] Magnetization in a saturated medium is everywhere homogeniously aligned in a same direction. See chapter 4 for explanation of magnetization.

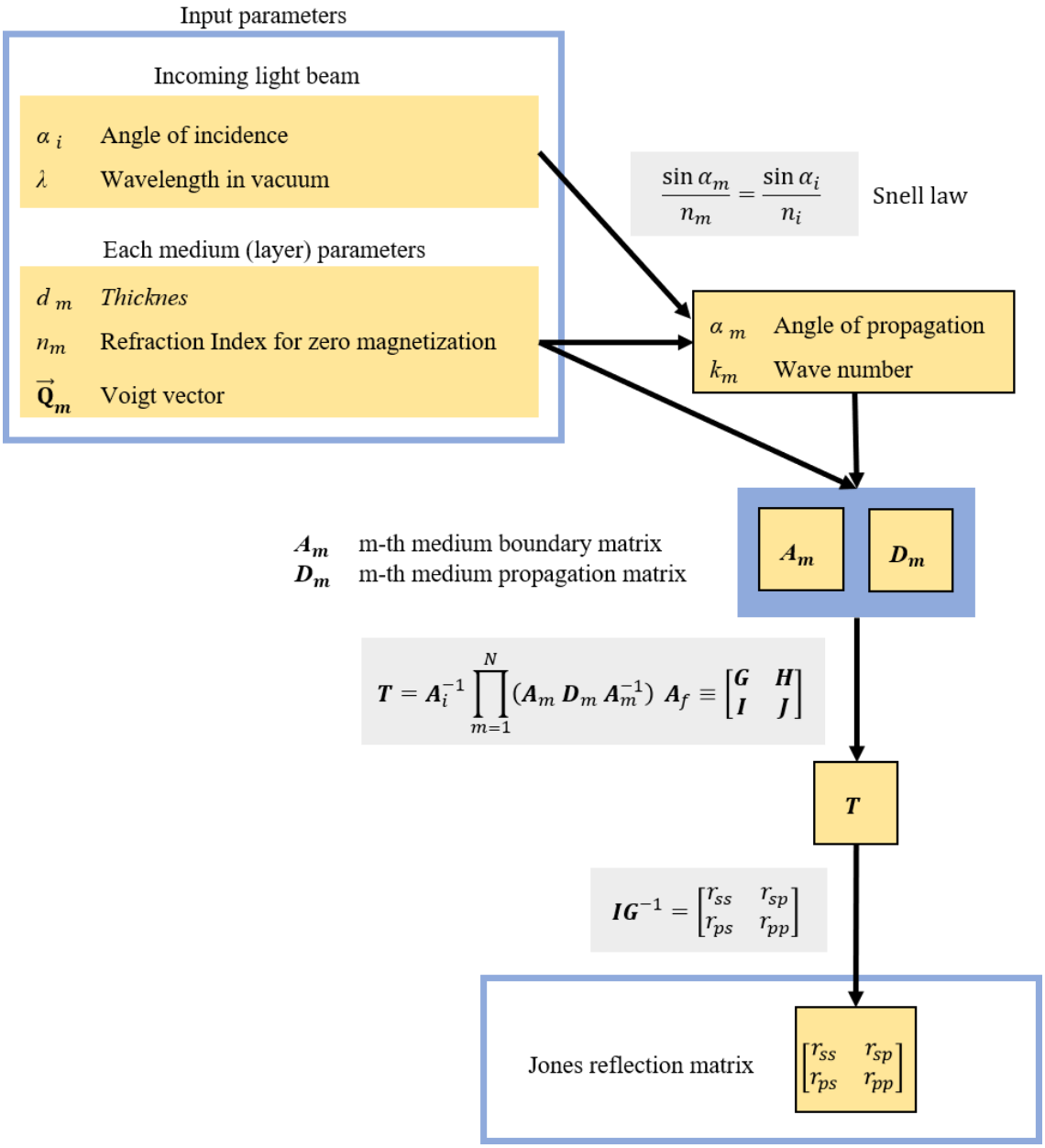

Figure 2.2 The scheme of computational process of the Jones reflection matric of a multilayer sample.

2.2.1 Step 1: Input parameters

In the beginning, we need to know the input parameters. Here are two parameters related to the incoming light beam:

α_i The Angle of Incidence

λ Wavelength in vacuum

Then, we need several parameters for each medium where the light will propagate. The initial medium is usually air – here we need to know:

n_i Refraction Index

$\vec{\mathbf{Q}}_i$ Voigt Vector (it is equal to zero vector in the air)

Voigt vector is a new term. We can take it as a vector containing three components carrying information about medium anisotropy which is caused by magnetization.

After the initial medium, a light comes to our sample composed of various layers of various materials. For each layer, we need its:

d_m Thickness

n_m Refraction Index

$\vec{\mathbf{Q}}_m$ Voigt Vector

m is a serial number of a layer ($m = 1, 2, 3$ ...).

The final layer is usually a thick substrate that cannot be shined through. Therefore, we do not need to know the exact thickness, but only:

n_f Refraction Index

$\vec{\mathbf{Q}}_f$ Voigt Vector

2.2.2 Step 2: Angles of Propagation and Wave numbers

The second step is to calculate the angle of propagation α_m and wavenumber k_m for each layer. Propagation angle can be received by Snell refraction law:

$$\frac{\sin \alpha_m}{n_m} = \frac{\sin \alpha_i}{n_i} \tag{2.1}$$

and wave number can be calculated from wavelength in a medium λ_m by following equations (2.2), (2.3).

$$\frac{\lambda_m}{n_m} = \frac{\lambda}{n_i} \tag{2.2}$$

$$k_m = \frac{2\pi}{\lambda_m} \tag{2.3}$$

2.2.3 Step 3: Boundary and Propagation Matrices

The third step is to use all these parameters to compose *medium boundary matrix* ***A*** and *medium propagation matrix* ***D*** for each medium (for the initial and final medium, we make only **A** matrices).

$$\boldsymbol{A}=\begin{bmatrix} 1 & 0 & 1 & 0 \\ \frac{i}{2}\left[-Q_y\tan\alpha\ (1+\cos^2\alpha)+Q_z\sin^2\alpha\right] & \cos\alpha+iQ_x\sin\alpha & \frac{i}{2}\left[Q_y\tan\alpha\ (1+\cos^2\alpha)+Q_z\sin^2\alpha\right] & -\cos\alpha+iQ_x\sin\alpha \\ \frac{in}{2}\left(Q_y\sin\alpha+Q_z\cos\alpha\right) & -n & \frac{in}{2}\left(Q_y\sin\alpha-Q_z\cos\alpha\right) & -n \\ n\cos\alpha & \frac{in}{2}\left(Q_y\tan\alpha+Q_z\right) & -n\cos\alpha & \frac{in}{2}\left(Q_y\tan\alpha-Q_z\right) \end{bmatrix} \tag{2.4}$$

$$D=\begin{bmatrix} U\cos\delta_i & U\sin\delta_i & 0 & 0 \\ -U\sin\delta_i & U\cos\delta_i & 0 & 0 \\ 0 & 0 & U^{-1}\cos\delta_r & -U^{-1}\sin\delta_r \\ 0 & 0 & U^{-1}\sin\delta_r & U^{-1}\cos\delta_r \end{bmatrix} \tag{2.5}$$

$$U\equiv\exp(-ikd\cos\alpha)$$
$$\delta_i\equiv\frac{kd}{2}(Q_y\tan\alpha+Q_z)$$
$$\delta_r\equiv\frac{kd}{2}(Q_y\tan\alpha-Q_z)$$

These two matrices were introduced in [14]. We will try to explain their role in our calculation. Let us think about an electromagnetic wave reflecting on a sample, as demonstrated in figure 2.2. In the first medium (air), we have an initial wave traveling toward a sample and a reflected wave traveling away from the sample. These two waves can be described by electric intensities in *s* and *p* polarization. In this notation, both waves are represented by a ***P*** vector defined as:

$$\boldsymbol{P}\equiv\begin{bmatrix} E_s^i \\ E_p^i \\ E_s^r \\ E_p^r \end{bmatrix} \tag{2.6}$$

Now, we need to solve the change of electric fields after passing the first boundary (sample surface). Here we used boundary conditions derived from Maxwell equations:

$$E_{\parallel 1}=E_{\parallel 2}$$
$$H_{\parallel 1}=H_{\parallel 2} \tag{2.7}$$

Where $E_{\parallel 1}$ and $E_{\parallel 2}$ are electric fields parallel to the boundary between medium 1 and 2. $H_{\parallel 1}$ and $H_{\parallel 2}$ are magnetic fields parallel to the boundary between medium 1 and 2. To translate the ***P*** vector to variables in equations (2.7), we use matrix **A**:

$$\boldsymbol{A}\begin{bmatrix} E_s^i \\ E_p^i \\ E_s^r \\ E_p^r \end{bmatrix} = \begin{bmatrix} E_x \\ E_y \\ H_x \\ H_y \end{bmatrix} \tag{2.8}$$

Then, we need to solve changes of waves during the way between any boundaries *a* and *b* through a medium of defined thickness. This task is done by matrix ***D***:

$$\boldsymbol{D}\begin{bmatrix} E_s^i \\ E_p^i \\ E_s^r \\ E_p^r \end{bmatrix}_a = \begin{bmatrix} E_s^i \\ E_p^i \\ E_s^r \\ E_p^r \end{bmatrix}_b \tag{2.9}$$

2.2.4 Step 4: T Matrix

We know how to describe the influence of sample layer boundaries and also the influence of medium thickness. Now, we compose it all together into one matrix ***T***.

$$\boldsymbol{T} = \boldsymbol{A}_i^{-1} \prod_{m=1}^{N} (\boldsymbol{A}_m \, \boldsymbol{D}_m \, \boldsymbol{A}_m^{-1}) \; \boldsymbol{A}_f \equiv \begin{bmatrix} \boldsymbol{G} & \boldsymbol{H} \\ \boldsymbol{I} & \boldsymbol{J} \end{bmatrix} \tag{2.10}$$

2.2.5 Step 5: Jones Reflection Matrix

The last step is to express the Jones reflection matrix:

$$\hat{J}_R = \begin{bmatrix} r_{ss} & r_{sp} \\ r_{ps} & r_{pp} \end{bmatrix} = \boldsymbol{I}\boldsymbol{G}^{-1} \tag{2.11}$$

As soon as we have this Jones matrix $\hat{J}_R$, we can easily express Kerr rotation θ and ellipticity ϵ for initially *s* or *p* polarized light:

$$\begin{aligned} \theta_s + i\epsilon_s &= \frac{r_{ps}}{r_{ss}} \\ \theta_p + i\epsilon_p &= \frac{r_{sp}}{r_{pp}} \end{aligned} \tag{2.12}$$

2.3 Voigt Vector and Permittivity Tensor

Here, we come back to the Voigt vector and provide a better explanation. To find its meaning, we start at matter polarization ***P*** as explained in [12]**:**

$$\boldsymbol{P} = n_e\, e\, \boldsymbol{r} = \epsilon_0\, \hat{\boldsymbol{\chi}}_e\, \boldsymbol{E} \tag{2.13}$$

Here n_e is a number of charged particles (electrons) per unit volume, *e* is an elementary charge, and **r** is a displacement vector (connecting atomic core and center of its electron cloud, which could be displaced by external electric field ***E***). ϵ_0 is a vacuum permittivity, and $\hat{\boldsymbol{\chi}}_e$ is electric susceptibility tensor – expressing specific matter sensitivity to an external electric field. The equation (2.13) corresponds with reality only approximately, but in weak electric fields as electromagnetic waves, this formula is good enough.

Now, we define permittivity tensor (sometimes called dielectric tensor):

$$\hat{\boldsymbol{\epsilon}} \equiv \hat{\mathbf{1}} + \hat{\boldsymbol{\chi}}_e \tag{2.14}$$

The same permittivity tensor can be written in the following form[1]:

$$\hat{\boldsymbol{\epsilon}} \equiv \epsilon \begin{bmatrix} 1 & iQ_z & -iQ_y \\ -iQ_z & 1 & iQ_x \\ iQ_y & -iQ_x & 1 \end{bmatrix} \tag{2.15}$$

where ϵ is a permittivity scalar constant characteristic for particular material connected with optical refraction index *n*:

$$\epsilon = n^2 \tag{2.16}$$

In definition (2.15), we see components of Voigt vector defined as:

$$\boldsymbol{Q} \equiv [Q_x \quad Q_y \quad Q_z] \tag{2.17}$$

Voigt vector is closely connected to sample magnetization ***M***:

[1] In this model, we consider only the linear Kerr effect and omit the second order Kerr effect. For example, we omit the influence of the transversal Kerr effect that can slightly change the polarization of *p*-polarized light and the result could be a mixture of longitudinal and transversal Kerr effect. Therefore, it is better to use *s*-polarized light, where the transversal Kerr effect can affect only reflection but not the polarization [23]. In our model, we also suppose that the medium is initially isotropic, and we neglect all anisotropy effect which are not caused by a magnetization.
We recommend [9] for more general derivation of the permittivity tensor and [24] for examples of second order Kerr effect.

$$\boldsymbol{M} = |\boldsymbol{M}| \; [m_x \quad m_y \quad m_z] \tag{2.18}$$

$$\boldsymbol{Q} = Q_0 \, [m_x \quad m_y \quad m_z] \tag{2.19}$$

Where $[m_x \quad m_y \quad m_z]$ is one unit vector in direction of the magnetization. Q_0 is a complex scalar Voigt constant characteristic for certain material and usually measured for saturated magnetization.

2.4 Numerical Calculations

One of the main advantages of this calculation method is its direct use in numerical calculations. Figure 2.3 is an example of a calculation of Kerr ellipticity and rotation dependence on the thickness of the magnetized medium. Mainly this can be used for thickness measurement [14].

Here we see that light can penetrate in the metal medium (here permalloy) at approximately 60 nm. Therefore, if we deposit more material under penetration depth, it does not influence reflected light.

The second interesting fact in Figure 2.3 is that the Kerr effect in the polar configuration is much stronger than in longitudinal.

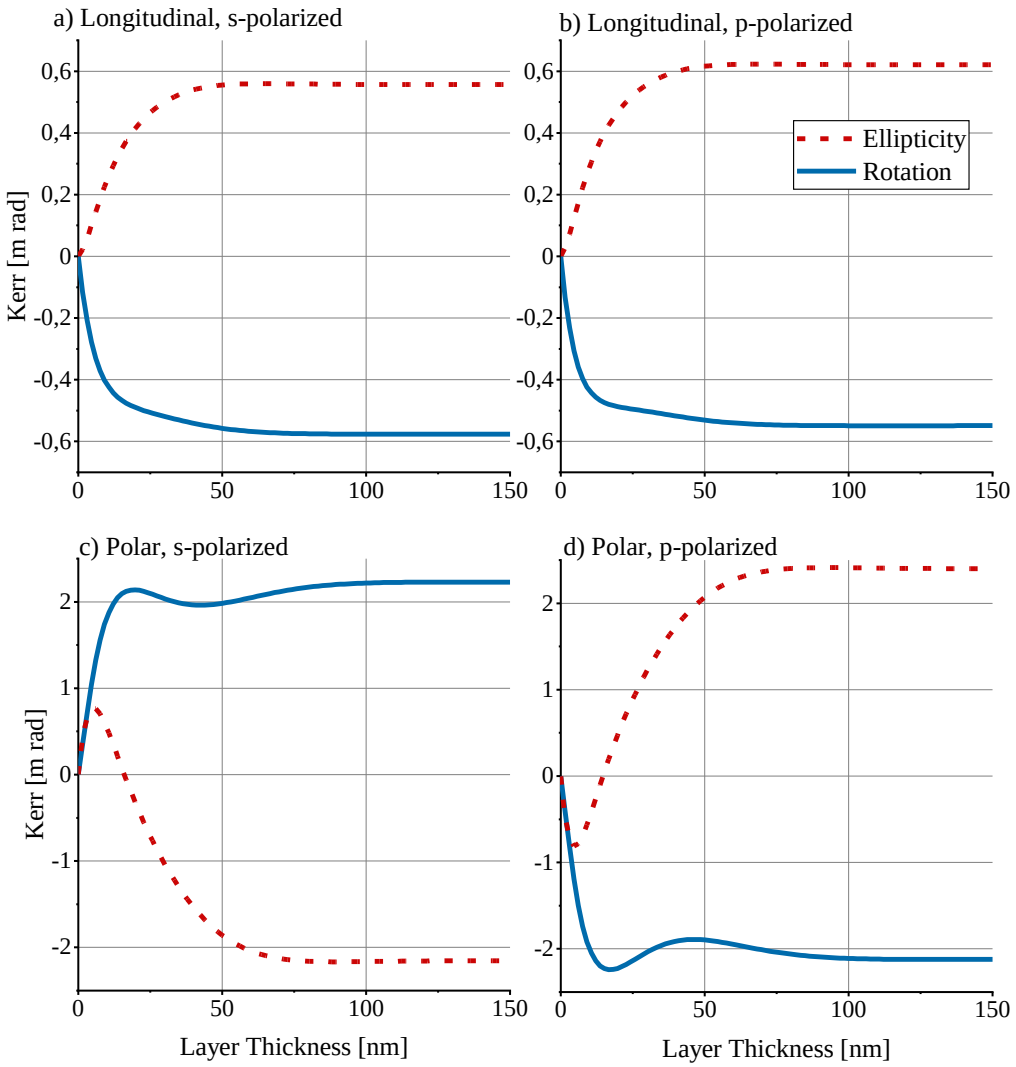

Figure 2.3 Simulated values of Kerr ellipticity and Kerr rotation in dependence on thickness of magnetic medium - permalloy layer. We have used following constants from [9]: wavelength λ = 633 nm, incident angle α_i = 0.5 rad, permaloy refraction index n =1.915+4.0256i, permaloy Voigt constant Q = 0.00492-0.01316i. Substrate is silicon with refraction index n = 3.678+0.005.

In the paper [14], the Voigt vector is handled as a free variable used to fit this simulation according to measured ellipticity and rotation. We recommend using the results of this simulation carefully since the calculation is very sensitive to the value of the Voigt constant.

We have discussed reflection on magnetized layers and the Kerr effect. We can also describe this phenomenon mathematically and find a suitable Jones reflection matrix.

3 Microscope – Optics and Analog Signal Processing

We are done with a theoretical introduction, and we turn to practical work, to Kerr microscope Miranda version 5.0.

First, we introduce the general principles of Kerr microscopy and their variety. Then, we look in detail at optics and analog signal processing of the microscope Miranda.

3.1 Kerr Microscopy

A Kerr microscope is an optical microscope utilizing the Kerr effect to show the magnetization of an observed sample. To reach a high resolution, all light is focused by the objective. This enables us to observe also small magnetic structures and domains.

There are two main kinds of Kerr microscopes: wide-field and laser-scanning.

Table 3.1 The way of light in Kerr microscopes.

	Laser-scanning microscope	Wide-field microscope
Light Source	Laser	Light Emitted Diode
Polarizer	Linear Polarizer	Linear Polarizer
Objective	Infinite-corrected	Infinite-corrected
Sample		
Objective again		
Optional Optics	HWP, QWP[1]	HWP, QWP
Analyzer	Wollaston Prism	Linear Polarizer
Detector	Photodiode	CCD chip

In wide-field microscopes, a light source is incoherent, usually a diode. This light is polarized by the linear polarizer and focused by the infinite-corrected objective into inspected position on the sample. Here, the light covers the whole field of view and is reflected back to the objective. The objective collimates the light again into the beam, which is deflected by a beamsplitter to an analyzer – the second linear polarizer rotated over 90° relatively to the first one. Only that light fraction that was rotated by the Kerr effect while reflection can pass. In the end, this remaining light is detected by a CCD camera[2] that displays an image to the user. The image is usually in grayscale, where intensity is proportional to magnetization in a chosen direction. We recommend an article from Soldatov and Shäfer [8] for more information about wide-field Kerr microscopy.

[1] QWP is a quarter wave plate, HWP is a half wave plate.
[2] CCD chip is based on CCD chip (Charge Couple Device) which is a photodetector consisting from a net of many photodiodes.

On the other hand, laser-scanning Kerr microscopes employ laser as a light source. The laser beam does not cover the whole field of view on the sample, but only one spot. Therefore, we do not need a CCD chip but only two[1] diodes to detect the reflected light. Scanning microscopes can use Wollaston prism as an analyzer.

The disadvantage that a scanning microscope can inspect only one spot on a sample at one time is compensated by a higher signal-to-noise ratio from this single spot. Scanning microscopes can use Wollaston prism as an analyzer. This enables them to do a quantitative measurement of Kerr rotation or ellipticity. Rotation and ellipticity are proportional to magnetization, and their values can be normalized. Since we usually know saturation magnetization for a particular material, we can also find values of components of the magnetization vector. Only laser-scanning Kerr microscopes can do quantitative measurements.

3.2 Miranda Microscope Overview

Here, we want to briefly describe the essential functions of our scanning microscope called Miranda. The scheme of Miranda is imaged in Figure 3.1.

An observed sample lies on a stage that can move along all three axes, *x, y, z*, and rotate the sample around the vertical z-axis. The electromagnet creates a magnetic field, which is applied to the sample. Miranda has a He-Ne laser. The laser beam is focused on the sample by an objective. Finally, the reflected laser beam is measured by quadrupole-diode detectors. Users can watch the sample surface thanks to an additional white light illumination and camera.

The microscope is fully automatized and controlled by a computer. The computer controls the electric current in magnetic coils and the movement of the stage. It also processes amplified data from optical detectors, a camera, and a Tesla-meter.

[1] We use 4+4 diodes (two four-quadrant detectors), because we simultaneously detect all three components of magnetization.

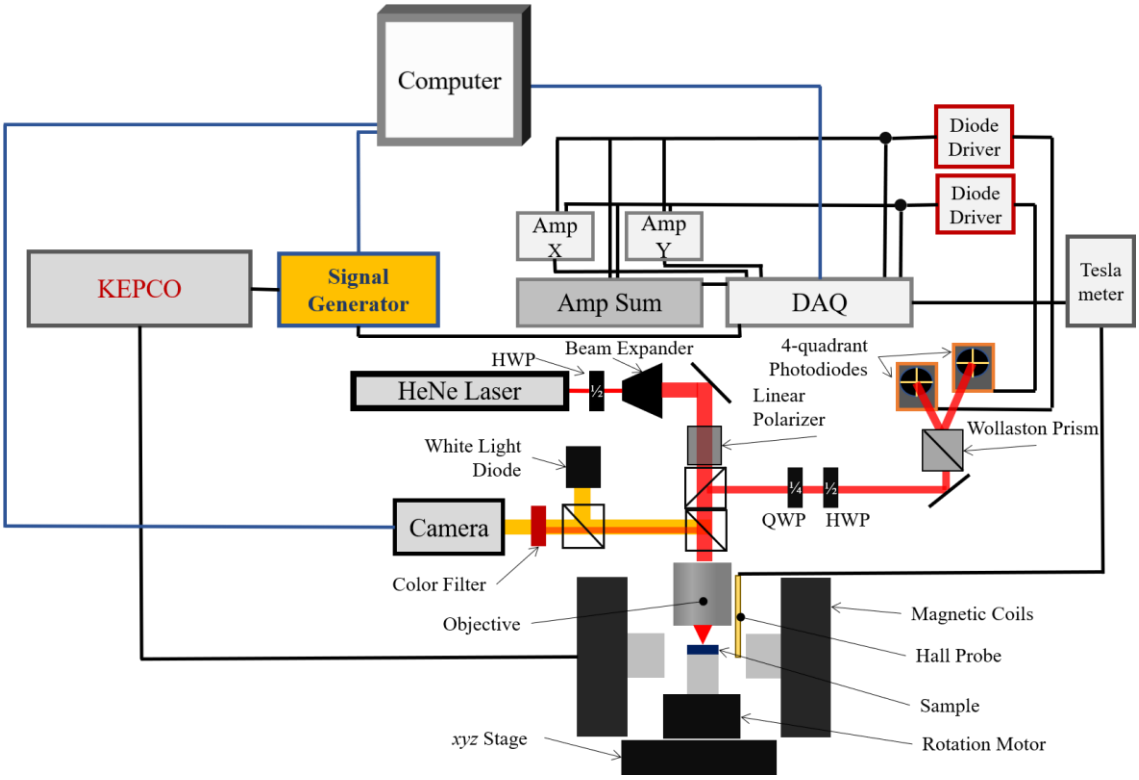

Figure 3.1 Complete scheme of Miranda microscope optical and signal processing system. A laser beam is red-colored. The white diode light beam is colored yellow. Coaxial cables and double conductor lines are colored black. USB communication cables are colored blue.

3.3 Laser Optics of Miranda

This section goes into detail along the trajectory of laser light in the Miranda microscope and describes all used optical components.

3.3.1 He-Ne Laser

We use Helium-Neon laser emitting red light at 632.8 nm wavelength. The original laser beam is 1mm in diameter and is almost linearly polarized. The measured polarization is in Figure 3.2.

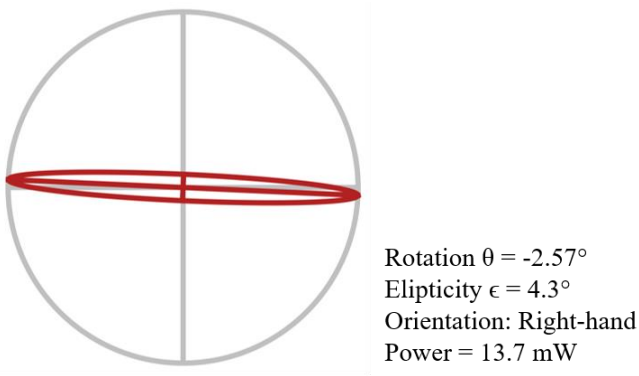

Figure 3.2 Measured polarization by a polarimeter. The laser beam from HeNe laser (after double reflection at periscope).

3.3.2 Half-Wave Plate

A half-wave plate is used to rotate the plane of linear polarization at an arbitrary angle. This is used to avoid losing intensity on the following polarizer.

3.3.3 Beam Expander

The beam expander expands the beam diameter from 1 mm to 5 mm. We have aligned this expander using a shearing interferometer to create the best-collimated beam.

3.3.4 Mirrors

Most of the used mirrors for changing the direction of the beam are dielectric.

3.3.5 Linear Polarizer

Glan Thompson crystal linear polarizer can be rotated to set the arbitrary angle of the plane of polarization. We use polarization perpendicular to the external magnetic field as in Figure 3.3. This enables us to measure the most important longitudinal magnetization without transversal Kerr influence. Unfortunately, the measurement of transversal magnetization can be slightly affected by magnetization in the longitudinal direction (second-order Kerr effect).

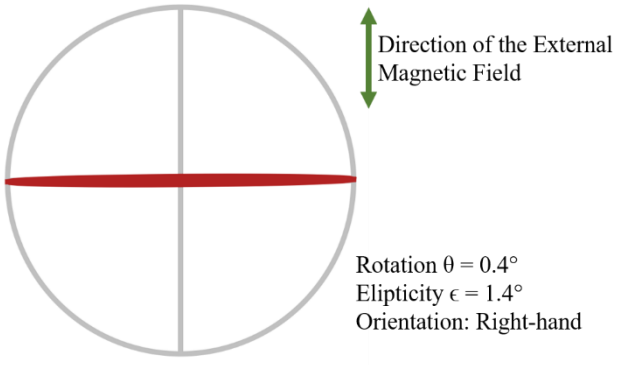

Figure 3.3 Measured polarization of the laser beam before it reaches the objective. The beam was polarized by the linear polarizer perpendicularly to the external magnetic field. If we consider the

sub-beams (1,2) probing longitudinal magnetization, we see in this Figure that the incident plane is parallel to the external magnetic field, and the beam is s-polarized.

3.3.6 Objective

The laser beam passes two beam splitters and comes to the infinite corrected objective. The objective is made by Zeiss (item number 422492-9960). Its magnification is 100x, and its working distance is 4.1 mm.

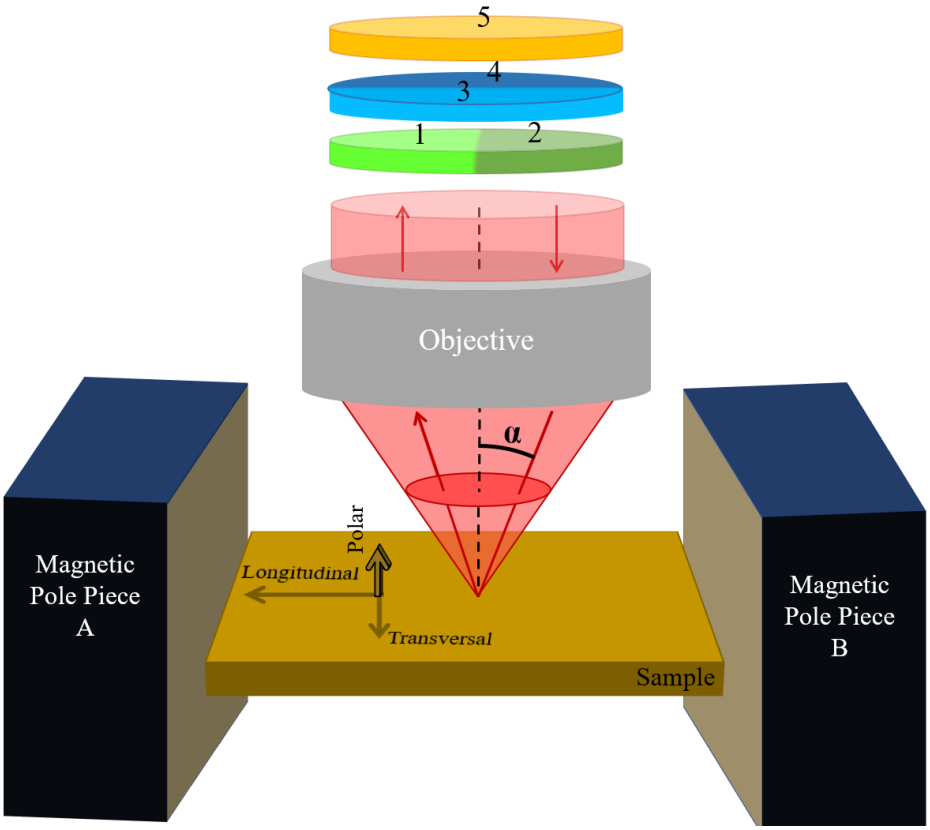

Figure 3.4 Laser covers the whole top entrance aperture of the objective. Such a wide beam is focused on the sample surface under a wide range of incident angles α. This makes a laser light cone above the focused spot. The maximal incident angle is 48.6°. We draw a trajectory of one representative ray in the laser beam. The top color circles demonstrate five sub-beams carrying specific information about magnetization. 1,2 are sensitive to the longitudinal magnetization, 3,4 to the transversal, and 5 to the polar. In the left part of the sample image, there are illustrated three directions of three basic magnetizations: longitudinal, transversal, and polar.

Thanks to the beam expander, the laser light covers the whole entrance aperture, and the laser light is focused on the sample over a wide range of incident angles α. This is very important because the Kerr effect appears only if the dot product of the lightwave vector and magnetic field is not zero. We can calculate the maximum angle α from the numerical aperture (*NA*) of the objective:

$$NA = n \sin(\alpha). \tag{8.1}$$

Here n is a refraction index that is approximately equal to one in air. According to the manufacturer, the *NA* of our objective is 0.75. Therefore, the maximal incident angle α is 48.6 degrees. This is demonstrated in Figure 3.5.

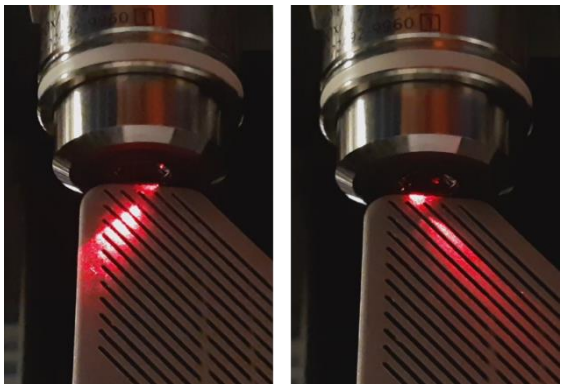

Figure 3.5 Measurement of maximal incident angle. The grid under the objective has 45° stripes. The laser beam can be tilted by objective up to 48.6°.

We can define five sub-beams carrying specific information about the sample magnetization in the reflected beam. They are pictured in Figure 3.4 as color circles. The sub-beam number 1 comes to the objective near the magnetic polepiece *B* and is reflected toward the opposite side, near the polepiece A and goes out of the objective on the left side. Since this sub-beam number 1 hits the sample in the plane of incidence parallel to the external magnetic field, its polarization was changed by magnetization, which is also parallel to the external magnetic field, and we can say that this sub-beam caries information about "longitudinal" magnetization written in its polarization change.

Sub-beam 2 undergoes the same polarization change as sub-beam 1 but with the opposite sign. Therefore, if we take a polarization difference of sub-beams 1 and 2, we get a twice stronger change caused by longitudinal magnetization, and all other changes will be canceled.

Sub-beams 3 and 4 have the plane of incidence perpendicular to the external magnetic field, and they are sensitive to the magnetization, which is also perpendicular to the external magnetic field. We call it "transversal" magnetization.

Sub-beam 5 is the whole beam itself. In this sub-beam, all incident angles α cancel each other, and we can consider this sub-beam as a single narrow ray of normal incidence. Sub-beam 5 is sensitive to the normal magnetization called "polar".

We use an infinity-corrected objective[1]. We send a collimated laser beam into the objective. Here it is focused into one spot on the sample, reflected, and then collimated again until it reaches detectors. But here arises a question: how large is the focused laser spot on the sample?

To find the size of the laser spot, we were measuring a reflected intensity while we scanned an edge of high reflecting permalloy structure on a low-reflecting silicon substrate. This method was also used by Lukáš Flajšman [9]. We suppose that the laser beam has a Gaussian distribution of intensity. We can fit the measured intensity by an error function which is a Gaussian primitive function. Then, if we choose the spot edge to require that the laser spot contains 68% of the intensity, the perimeter will be equal to the standard deviation σ of fitted Gaussian function. If we place a sample in the plane of the laser focus, the diameter will be 0.49 µm according to measurement, which is demonstrated in Figure 3.6. The value of the diameter tells us how large is the smallest possible area where the Miranda microscope collects data while measuring.

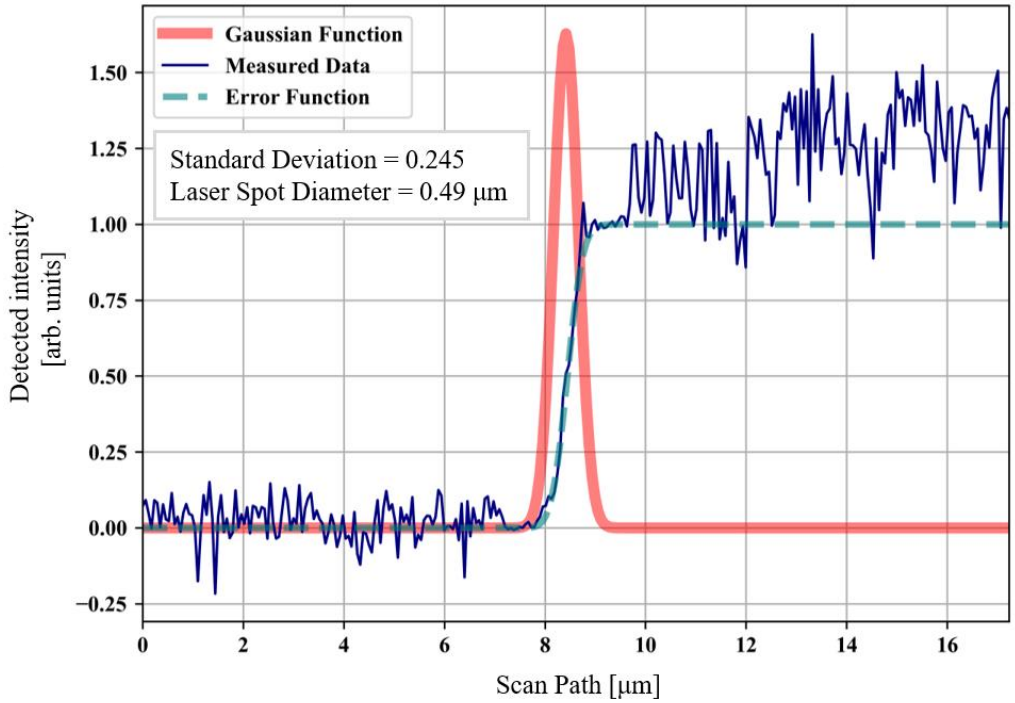

Figure 3.6 Measurement of the laser spot size diameter on the sample surface by scanning over the edge of a highly reflecting structure. Measured intensity is fitted by an error function. We suppose a Gaussian distribution of intensity in the laser beam, and the gaussian function is a derivative of the error function. The measured laser spot has a diameter of 0.49 µm, containing 68% of total intensity.

[1] An infinity corrected objectives have image plane in infinity.

3.3.7 Quarter Wave Plate

QWP can convert linear polarization to circular. See [17] for a detailed explanation. Using QWP is just optional. If we use it, we measure ellipticity. If we replace it, we measure rotation.

In the case of measuring ellipticity, we rotate by the QWP to create maximally circular polarization. Here, we used a polarimeter to find the best alignment.

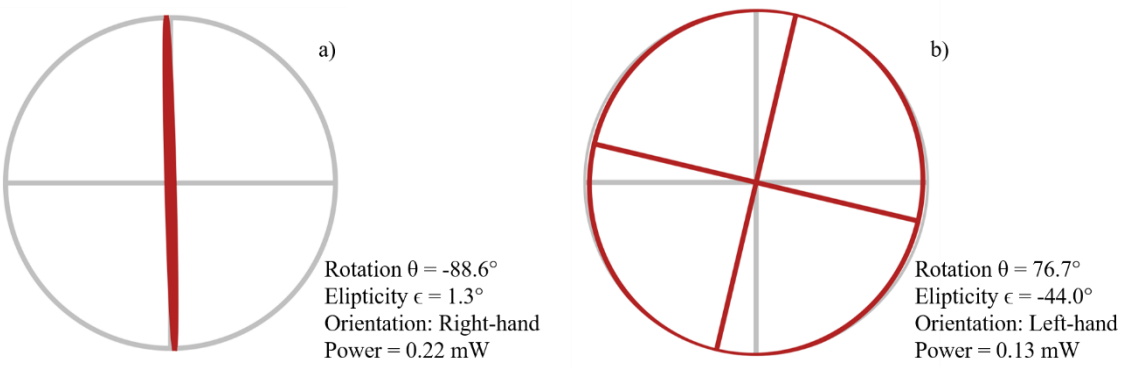

Figure 3.7 Measured polarization by a polarimeter after reflection on a sample: a) laser beam without QWP, b) beam correctly passed through QWP with correct alignment.

3.3.8 The Half Wave Plate

We align the HWP to rotate the elliptical polarization. We need to set the major axis to a horizontal or vertical position. We do this alignment at the end, according to the quality of the Kerr signal from sensors.

3.3.9 Wollaston Prism

Wollaston prism can split x-polarized and y-polarized components of the beam and tilt them 45° to each other. We have generally elliptically polarized light with a major axis in the *x* or *y* direction, and we need to split it into two beams of approximately the same intensity. Therefore, we rotated the Wollaston prism 45°.

With this alignment, both split beams should be theoretically identical, and only the Kerr effect can cause a difference.

3.3.10 Four-Quadrant Detectors

A reflected laser beam carries five information channels.

A four-quadrant detector is composed of four diodes. Each of two split beams is detected by such a four-quadrant detector. The detector's output is a voltage proportional to the detected intensity of light. This measuring system offers information about intensity in three ways at each detector:

Table 3.2 Three information channels about intensity differences. Numbers in round brackets correspond to numbers of sub-beams in Figure 3.2.

Manufacturer Sign	Intensity result	Source
x-difference	Left minus Right part of the beam (1,2)	Longitudinal Kerr
y-difference	Upper minus Lower part of the beam (3,4)	Transversal Kerr
Sum	Sum of all four quadrants (5)	Polar Kerr

3.4 Camera Imagining

In the Miranda microscope, we use white light to visualize the surface of the observed sample. As before, we go along the path of the white light as drawn in Figure 3.1.

3.4.1 Single LED Source

The source of the white light is a single white LED. The emitted light is focused by a lens.

3.4.2 Objective

The system of beam splitters leads the white light into the objective. We focus the image of the LED source to the back aperture of the objective to create Köhler illumination [18] of a sample. Then, it is reflected back on the sample surface. White light covers a much larger area than laser and illuminates a wide circle area around the laser spot.

3.4.3 High Pass Filter

We use an optical high pass filter to not allow laser light comes to the camera. This filter is transparent for light with a higher frequency than 500THz (600nm). All lower frequencies, including laser (632.8 nm), are blocked. This helps our software process sample images without a bright laser spot in the middle.

3.4.4 Camera

Light is focused on the camera CCD chip by a tube lens. The camera image is essential for a user to see the surface of the image and find the desired place which should be measured by the laser. Also, auto-positioning software uses this image for automatic measurement.

3.5 Signal Processing in Miranda Microscope

Here, we look at magnetic field control and then at the processing of the measured signal from detectors.

3.5.1 Magnetic field

The sample is surrounded by a magnetic field, which is parallel to the sample surface. We usually create a periodically oscillating magnetic field to measure hysteresis loops. For this purpose, we need such a field amplitude that forces the measured sample to magnetic saturation. To do this, we need a field up to 20 mT.

We use the KEPCO power supply to generate an electric current in the magnetic coils. The current is driven to flow periodically as a sinusoidal function with arbitrary frequencies up to 30 Hz.

Users can set any frequency and magnetic field intensity by a signal generator that controls KEPCO. This signal generator sends also trigger pulses to the DAQ (Data Acquisition card). Trigger pulses have the same frequency as the magnetic field, and they are used to synchronize signal measurement in DAQ.

We measure the magnetic field by Hall probe near the sample. An Analog signal from the tesla-meter device is connected to the DAQ.

3.5.2 Amplifiers

Signals from four-quadrant detectors are processed in three differential amplifiers as described in Table 3.3.

Table 3.3 Overview of three differential amplifiers operation. Longitudinal, transversal, and polar Kerr are either rotation (measurement without QWP) or ellipticity (measurement with QWP).

Amplifier	Input signal voltage	Analog operation	Output signal voltage proportional to:
Amp X	Left detector: x-difference Right detector: x-difference	Differentiating Gain 100	Longitudinal Kerr
Amp Y	Left detector: y-difference Right detector: y-difference	Differentiating Gain 100	Transversal Kerr
Amp S	Left detector: Sum Right detector: Sum	Differentiating Gain 10	Polar Kerr

Output amplified signals are led to the DAQ, which is connected to the computer via USB.

We experienced that it is essential to do differentiating operations analogically as we do in amplifiers. The resulting signal quality and operational speed are incomparable better than results acquired by digital differentiation.

4 Microscope - Mechanical Design

This chapter describes the mechanical construction of the microscope Miranda. First, we generally describe the assembly, and then we describe the stage, objectives, and magnet in detail.

The microscope is built on an optical table with vibration damping. Here are all optics, sample stage, and magnet. Other devices as the power source, amplifiers, drivers, and a computer are placed above the table.

The microscope itself has two floors, as pictured in Figures 4.1 and 4.2. The lower one is directly on the table surface. Here are laser, magnet, sample stage, and objective positioner. The upper floor is built on a thick aluminum breadboard that stands on three legs. Here are the remaining optics: laser expander, QWP, HWP, Wollaston prism, and four-quadrant detectors. Here is also visualization optics: white LED and camera. This upper floor is usually enclosed by a cover, which protects the optics against dust, surrounding light, and vibrations.

Most of the optics and construction components were provided by the Thorlabs company.

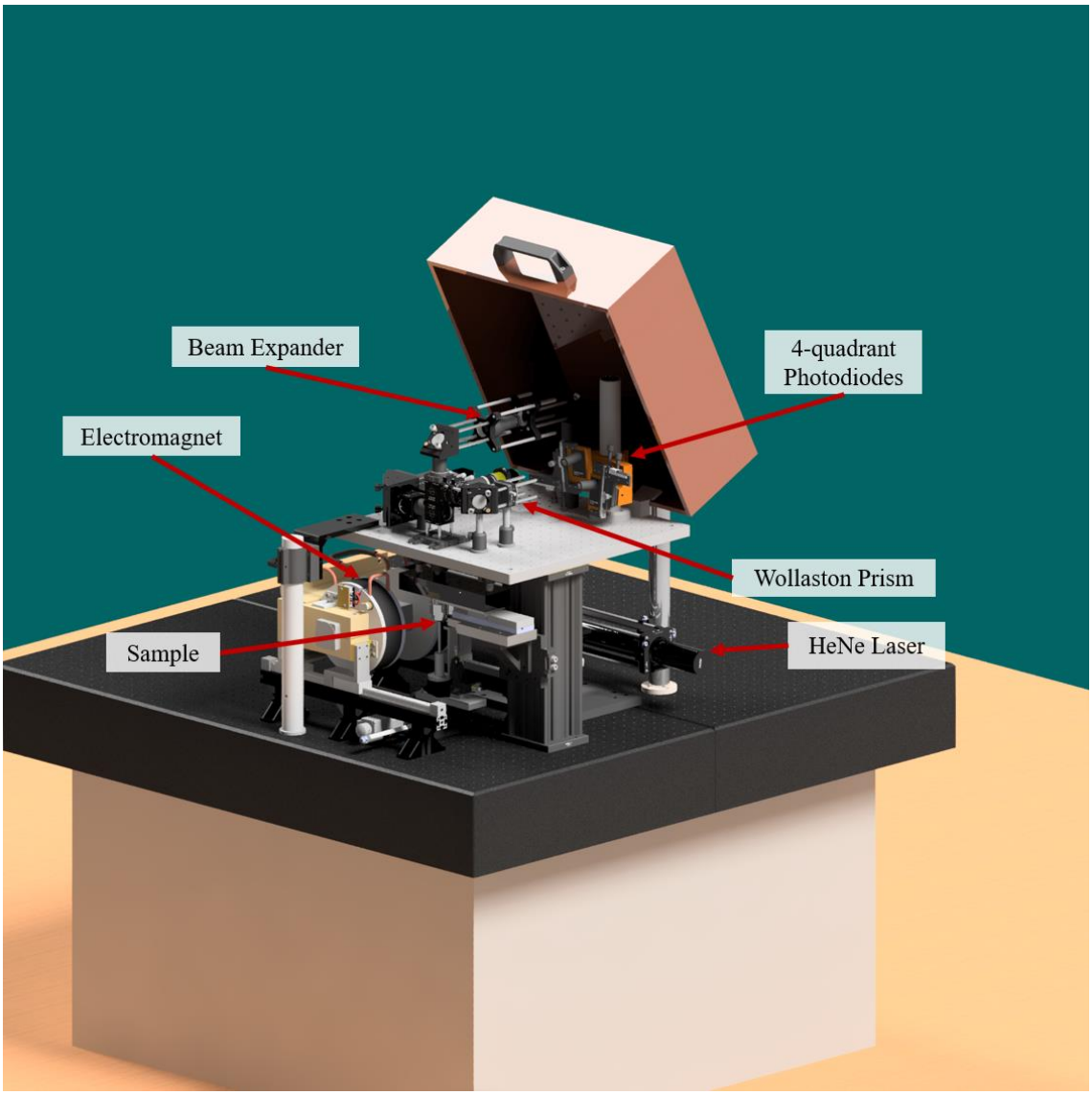

Figure 4.1 Rendered model of the microscope Miranda.

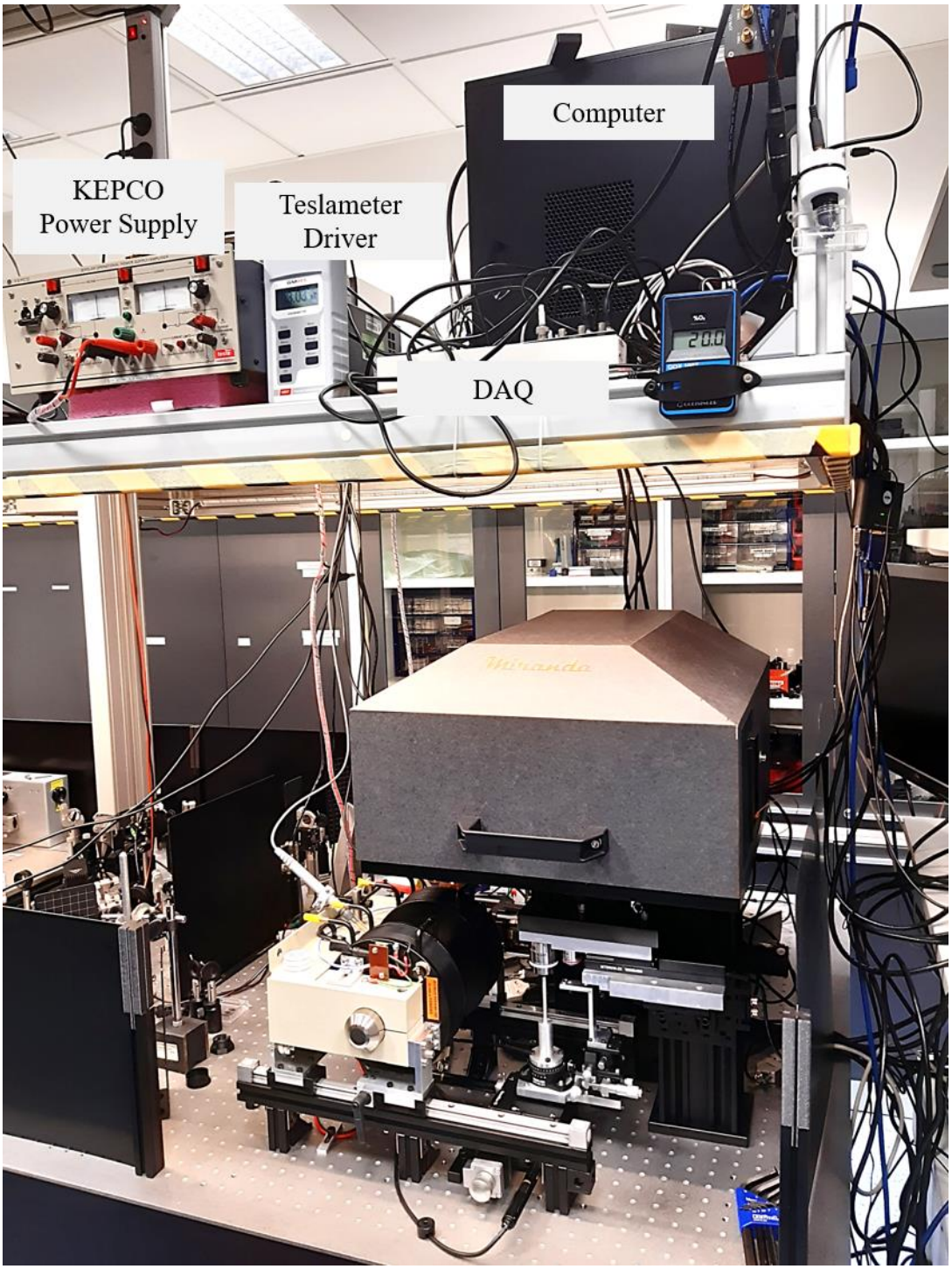

Figure 4.2 Microscope Miranda photo overview.

4.1 Sample Stage

All movements of a sample are performed by the motorized stage. The primary stage enables movement along three cartesian axis *x,y,z,* all in the 4 mm range. This is done by three stepper motors. For more delicate movements, we use three additional piezo positioners with a range of 21 μm, and resolution 20 nm.

On top of this primary stage, there is a rotational stepper motor that can rotate the sample over 360°. Thanks to the rotation, we can position structures on a sample at an arbitrary angle relative to the external field which is created by a magnet. A cylindrical sample-holder is placed on the top of the rotation motor. The sample holder is designed for samples that are 5x5 mm.

4.2 Objectives

Microscope Miranda has two objectives. This is pictured in Figure 4.3. The smaller one magnifies 8-times and can be used for the initial sample overview and for contacting a probe[1]. This objective also has a very long working distance which creates space for placing a sample on the stage below the objective.

The second larger objective magnifies 100-times and is used for the measurement. Changing the objectives is done by a linear stage which is powered by a stepper motor.

If a user wants to observe extraordinarily high samples (approximately up to 4 mm), objectives can be moved up. This must be done manually.

[1] The picoprobe contacting is described in the chapter 6.

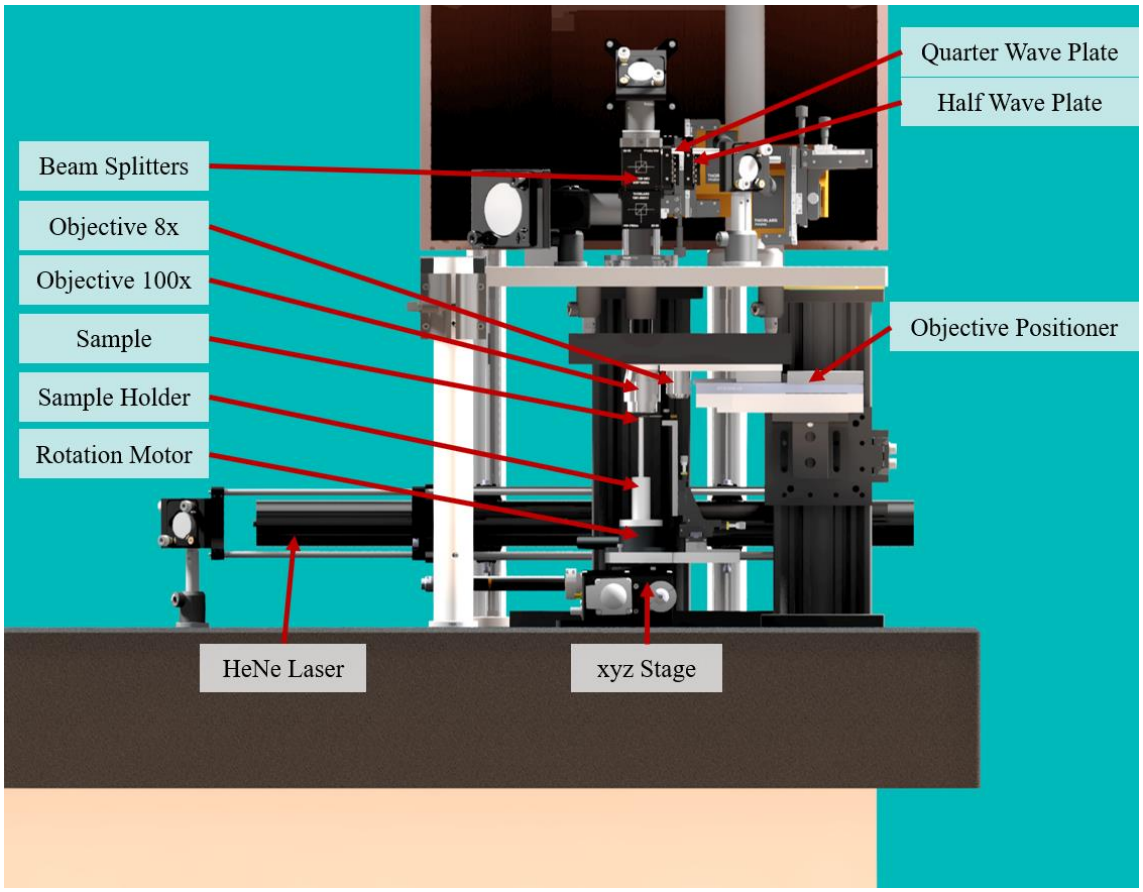

Figure 4.3 Front view of the microscope. Here, the magnet is removed to make the stage visible.

4.3 Electromagnet

We need to create a magnetic field around the observed sample. This is done by an electromagnet. This electromagnet stands on two rails and can be removed if a user wants to change a sample. This provides the user with enough operating space. The gap between the polepieces can be adjusted according to the size of a sample. We usually use the 10 mm gap. The smaller the gap, the stronger the magnetic field can be achieved with the same current. Figure 4.4 is a photo of a sample in a magnetic field which is measured by a Hall probe.

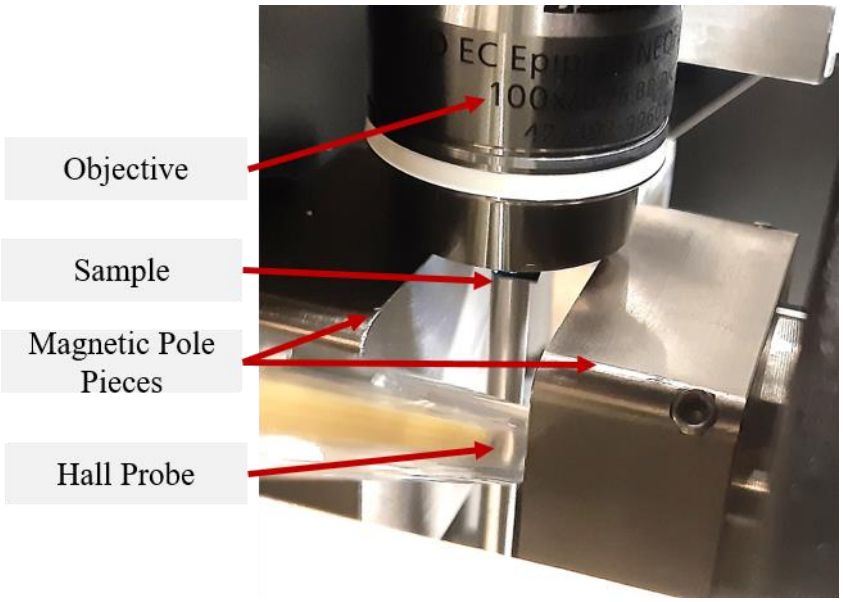

Figure 4.4 The photo of a sample between two magnetic polepieces.

5 Software and measurement

We designed this microscope to perform an automatic measurement, which is controlled by a computer. In this chapter, we introduce the Thatec software system and the processing of measured data. In the end, we show several examples of measurement.

5.1 Thatec

The THATec Innovation GmbH company develops a universal software system for the automatization of measurements. The general idea is to create a control module for each device employed in an experiment and then connect all these devices into one control interface, which is called ThatecOS. Here user can set all parameters of measurement and then run it automatically. Because measurements last up to several hours, it is beneficial to do them without the continual presence of a user.

While using Thatec, a user can quickly modify experiments and quickly learn to operate new devices which are controlled by the same system from Thatec.

In the case of the microscope Miranda, we cooperate with the Thatec company to modify their microscopy module to control our stage. The microscopy module controls *yxz* movements and rotation. The module uses camera image to perform auto-positioning, which we use to scan areas or stabilize during rotation.

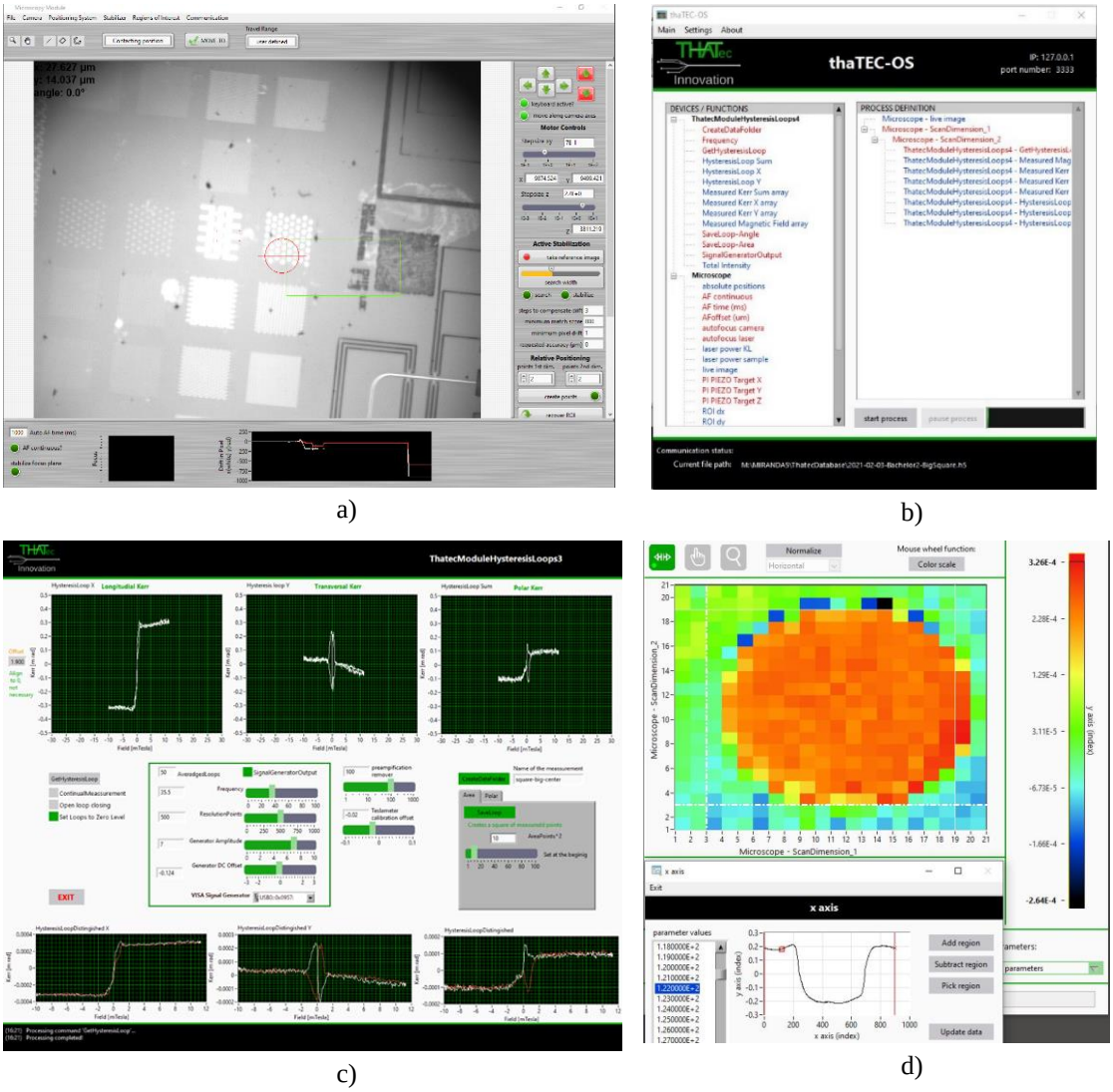

Figure 5.1 a) Thatec Microscopy Module - graphical user interface. The red cross in the middle shows the position of the laser spot. b) Thatec-OS - Central program interface to control all partial modules and drives the measurement process. c) Data Module for Hysteresis Loops - this module controls magnetic fields and processes data from detectors to measure hysteresis loops of longitudinal, transversal, and polar magnetization. d) Thatec Data Inspector - Database reader to display measured data. We see a longitudinally magnetized permalloy circle of diameter 8 µm.

5.2 Data processing

We need to proceed a raw data that is coming from detectors to a computer via a DAQ device[1]. This task is done by our hysteresis loops module. This module collects data from DAQ and controls the magnetic field via the signal generator.

[1] DAQ device is a system of voltmeters that converts analog signal from detectors to digital data that are sent to a computer.

The module usually repeats each measurement periodically five to one hundred times and takes the resulting average. Thanks to this process, random influences are suppressed, and the signal is enforced.

So far, our data from photodiodes are just voltage proportional to Kerr ellipticity or rotation. But we want to know the exact Kerr ellipticity (or rotation) value. We solve this problem according to Lukáš Flajšman [9].

The first equation (5.2) describes a case when we do not use a quarter-wave plate and measure Kerr rotation θ. The second equation (5.3) describes a case when we use a quarter-wave plate to measure ellipticity ϵ.

Without QWP $$-\frac{I_{\mathrm{dif}}}{2I_{\mathrm{sum}}} = \theta - 2K \tag{5.2}$$

With QWP $$-\frac{I_{\mathrm{dif}}}{2I_{\mathrm{sum}}} = \epsilon - 2K \tag{5.3}$$

These two equations contain two values of measured light intensities: I_{dif} and I_{sum}. We use the output voltage values from differential amplifiers[1] as I_{dif}. Then we use sum voltages from the two detectors and add them together to receive a value that can be used as I_{sum}. K is a constant value that is approximately equal to the angle of the half-wave plate in our setup. Usually, we want to align our setup to K equal to zero. This can be achieved by suitable rotation of HWP.

These two equations are derived by the small-angle approximation, which satisfies our measurement. They are valid for all three channels (longitudinal, transversal, and polar magnetization) measured on the setup:

Sample – (QWP) – HWP – Wollaston Prism – Photodetectors

Since we consider only the linear Kerr effect as mentioned in chapter 2, we concluded that the magnetization of an observed sample is proportional to the rotation and ellipticity. We can demonstrate this feature at the Faraday effect, which shares the same principle as the Kerr effect. Faraday effect is a change of polarization of a light beam while transmitting through a magnetized medium. The Faraday rotation θ and ellipticity ϵ are calculated by following equation [14]

$$\theta + i\epsilon = \frac{\pi L}{\lambda}(n_L - n_R) = -\frac{\pi L n}{\lambda}\boldsymbol{Q}\cdot\hat{\boldsymbol{k}}. \tag{5.3}$$

[1] We must divide the voltage value by an appropriate amplifier gain, since we detect I_{dif} just after aditional amplification which would change the ratio: $I_{\mathrm{dif}}/I_{\mathrm{sum}}$.

Here L is a distance that the light has traveled through the medium, λ is a light wavelength, $\boldsymbol{Q}$ is a Voigt vector, $\widehat{\boldsymbol{k}}$ is the unit vector along the direction of the light propagation, and n is the refraction index in the absence of magnetization. n_L and n_R are refraction indexes of left and right circularly polarized light:

$$n_L = n\left(1 - \frac{1}{2}\,\boldsymbol{Q}\cdot\widehat{\boldsymbol{k}}\right)\ , n_R = n\left(1 + \frac{1}{2}\,\boldsymbol{Q}\cdot\widehat{\boldsymbol{k}}\right). \tag{5.4}$$

Q depends on the magnetization according to equation (2.18).

If we want to know the value of the observed magnetization *M*, we can multiply measured rotation or ellipticity by an appropriate constant C.

$$\theta\ C_\theta = M\ ,\ \ \epsilon\ C_\epsilon = M \tag{5.5}$$

The value of C depends on the material and the way of measurement[1], but we usually know the value of the saturation magnetization of the material under investigation. Then we measure the Kerr rotation or ellipticity of this magnetically saturated sample. With these two values, we can compute the constant C from (5.5) and then use it to evaluate the whole range of magnetization.

5.3 Experimental Results of the Scanning Mode

In this section, we first introduce a scanning mode and then look at several examples of measured data from the Miranda microscope in this mode. They demonstrate the current possibilities that Miranda offers to any user.

The scanning mode is helpful to scan a particular area on our sample. In the microscopy module, we cover the area by a net of points and then let Miranda measure the hysteresis loop in each of these points. The resulting data show us a three-dimensional orientation of magnetization in an arbitrary magnetic field. These data can be converted to an OVF format[2] file, which becomes a standard in micromagnetic simulation software (e.g., Mumax).

Now, we look at three examples of area measurement. The first is a square structure from the permalloy on the silicon in Figure 5.2. The square is of dimension 20x20 μm^{2,} and the height is approximately 50 nm. If we apply a strong field, magnetization in this structure is aligned parallel to the field. But if the surrounding field is weak, the structure splits into several magnetic domains.

[1] Rotation and ellipticity varies with an angle of incidence on a sample. In case of thin film sample, the layer thicknes influences the rotation and ellipticity.
[2] OVF means „OOMMF Vector Field“ For more information, see: https://math.nist.gov/oommf/.

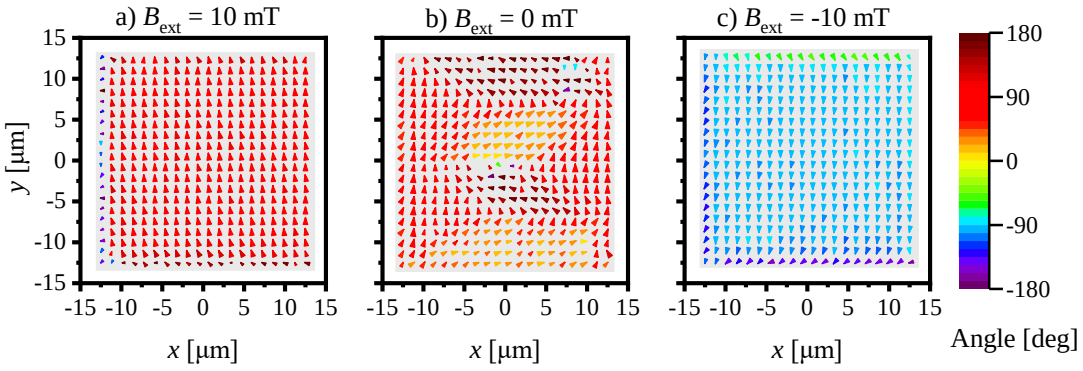

Figure 5.2 Area scan of a square permalloy structure of dimension 25 x 25 µm^2. a) The external magnetic field B_{ext} is 10 mT, and the magnetization is saturated in the longitudinal direction. b) B_{ext} is zero, and we see that the structure is divided into several magnetic domains. c) B_{ext} = -10 mT, and the whole structure is magnetized in the opposite direction compared to a).

The second measurement is on an 8 µm permalloy disk of the same height. Here we see very similar behavior, but in the weaker magnetic fields, the preferred magnetic orientation is a so-called vortex. Here, the magnetization is twisted parallel to the outer edge. The measured results are in Figure 5.3.

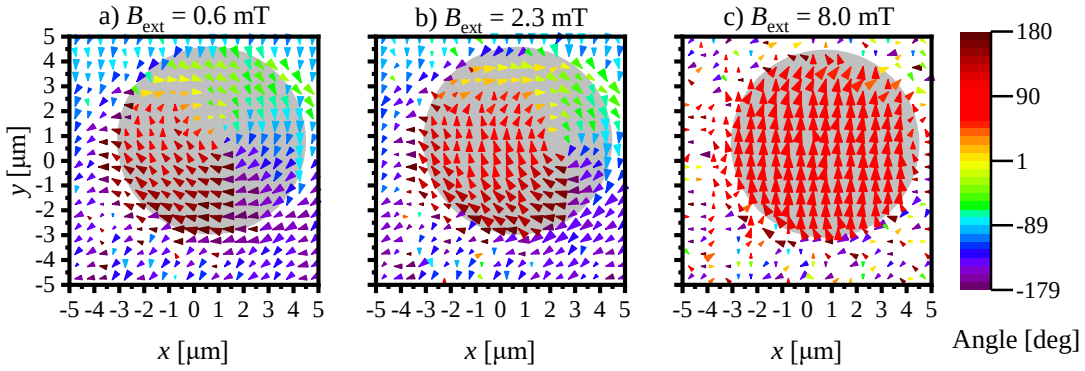

Figure 5.3 Area scan of a permalloy circle structure of diameter 8 µm. We see a vortex pattern of magnetization. a) Weak external magnetic field 0.6 mT. The vortex core is approximately in the center of the permalloy structure. b) Increasing magnetic field directs upwards in the picture. The area of the same upward magnetization grows and pushes the vortex core to the left. c) The vortex core is completely pushed out, and the whole structure is saturated by a relatively strong magnetic field 8 mT. Graph arrows that are outside of the structure do not relate with a Kerr signal.

The center of the magnetic vortex is the vortex core. In the hysteresis loop in Figure 5.4, which is measured in the center, we see sudden jumps which are caused by vortex core nucleation.

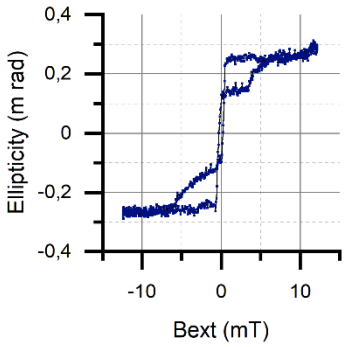

Figure 5.4 Hysteresis loop measured in the center of the previous disk. Sudden jumps in the loop correspond to nucleation and annihilation of the magnetic vortex core.

The third example of the area measurements is an iron-nickel flat structure on a copper crystal. This structure was created by Jakub Holobrádek. He prepared a continuous layer of metastable inverse permalloy FeNi, which is paramagnetic. Then, he transformed a square area of 20x20 μm^2 by a focused ion beam. In this way, he made a ferromagnetic square structure that consists of eight crystalographic regions, each with a different tilt of its lattice. More information is in the thesis of Jakub Holobrádek [19].

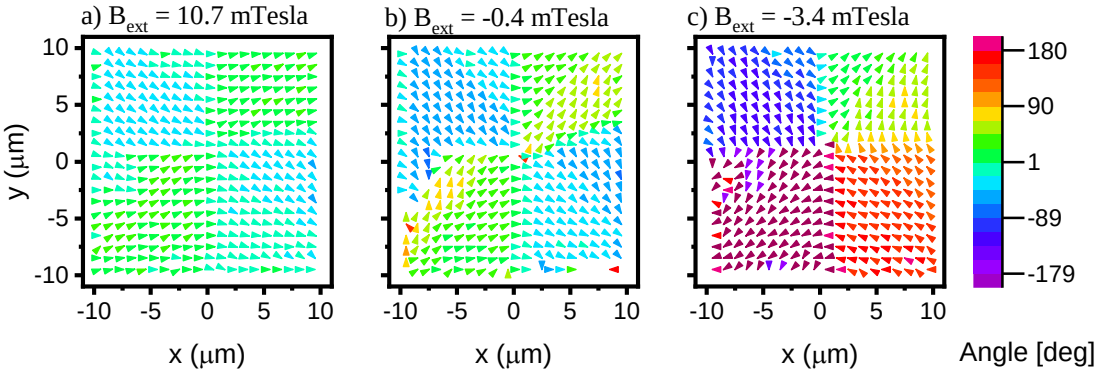

Figure 5.5 Area scan of a square iron-nickel structure. This structure consists of eight crystallographic regions with a different tilt of their lattice. In varying external magnetic fields, each crystal prefers another magnetization direction, which is caused by a strong anisotropy.

As we vary the external magnetic field, we observe the different orientations of magnetization in each crystalographic region. This is caused by a strong angular anisotropy. Magnetic angular anisotropy means that some directions of magnetization are more energetically efficient (easy axis) than the others (hard axis). Results are in Figure 5.5.

5.4 Experimental Results of the Rotation Mode

Very often, our samples have magnetic anisotropy. The behavior of their magnetization depends on the angle between their anisotropy axis and external magnetic field. This could be caused by the shape of the magnetic structure, crystallography, or some other effect.

In such cases, we can employ the rotation mode of Miranda. We find a certain position on the sample and then let the Miranda microscope rotate the sample over 360 degrees and measure a hysteresis loop with an arbitrary angular step. During this process, we use auto-positioning to keep the laser spot at the same place.

Here we look at one example of such a measurement. We measured a 5x5 mm^2 layer of iron-rhodium at a temperature of 127 °C. At this temperature, Iron-Rhodium becomes ferromagnetic[1]. In the results, we see a strong angular anisotropy which influences the width of hysteresis loops (change of a coercive field). This material has two hard (and two easy) axis of magnetization, which perform four peaks in our 360-degree measurement as we pass each axis twice. Experimental results are in Figure 5.6.

[1] This can be compared with [25].

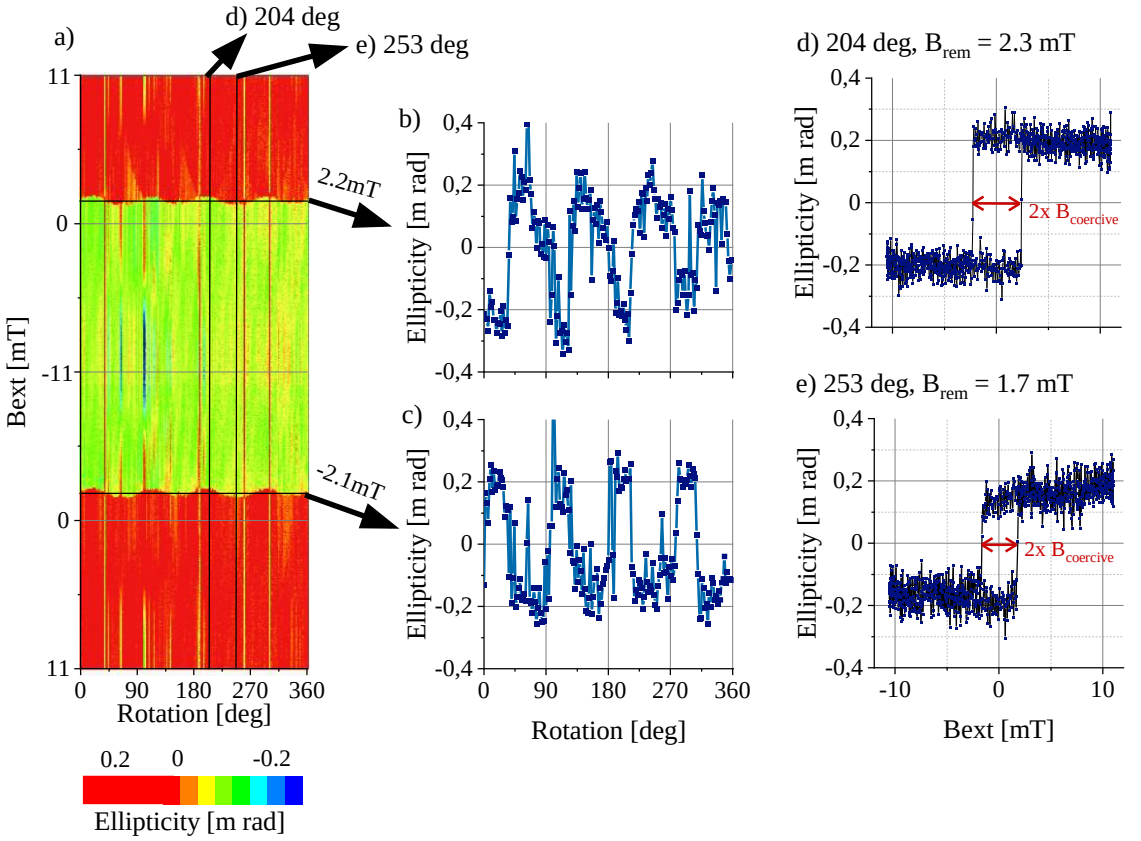

Figure 5.6 Rotational measurement of angular anisotropy of Iron-Rhodium layer at 127°C. a) All measured data plotted as an intensity graph. The scale was shifted to highlight switching of the magnetization. b) c) Measured Kerr ellipticity in dependency on the angle at specific magnetic fields: 2.2 and -2.1 mT. We see four maxima which correspond to the two easy axes in b) and hard axes c). The angle between the hard and easy axis is 45 degrees. d) Hysteresis loop measured along one easy axis (204 deg). We see a stronger coercive field – the loop is wide and rectangular. e) Hysteresis loop measured along a hard axis (253 deg). We see a 1.35 times weaker coercive field. The loop is narrower and rounder than at d).

6 Time Resolution

In this chapter, we want to introduce a pump-probe technique for measurements with temporal resolution. After that, we demonstrate this technique by observing an excitation of magnetic vortexes.

Many exciting phenomena are very fast [20], so fast that standard detectors cannot detect their temporal evolution. A straightforward example of fast phenomena is an oscillating vortex structure. The vortex was mentioned in the previous chapter, and we already know that its magnetization in a circular pattern aligns itself parallel along the edge. The central vortex core directs its magnetization perpendicular to the plane of the disc. Here, we excite this configuration from the equilibrium, i.e., we decentralize the magnetic pattern and shift the vortex core out of the center of the permalloy structure. It gets energy, and the core starts to oscillate around the center as a damped oscillator. We expect the oscillation frequency to be approximately 100 MHz (period 10 ns). We cannot detect these rapid changes by a standard approach used for static measurements. All that we detected would be an average intensity collected at photodiodes. But a pump-probe technique can solve this problem.

6.1 Pump-Probe

The Pump-Probe technique is widely used for a variety of measurements with a subnanosecond resolution. A phenomenon is periodically started by a pump. The pump is an electric pulse in our case, but generally, it could be anything else, e.g., laser pulse. Then, we send a probe. In our case, we use a laser pulse. The probe is synchronized with the pump with an adjustable but precious delay. The probe examines the actual state of the systém and brings this information to a detector. The detector can integrate the probing signal over many periods. As we change the probing delay, we observe the systém in variable time from the start of the phenomenon. This technique is pictured in Figure 6.1.

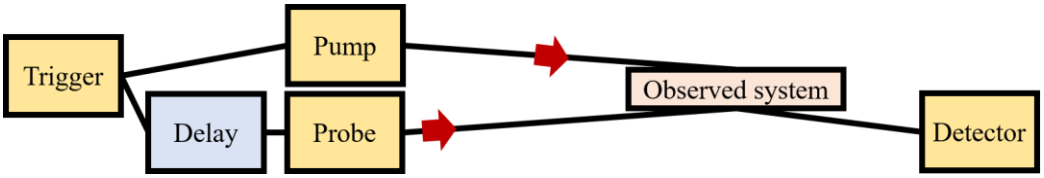

Figure 6.1 An general scheme of a pump-probe method.

The limiting factors of a temporal resolution are the temporal length of the probe and the synchronization precision.

6.2 Setup for the Time Resolution

We adjusted the microscope Miranda for measurements with a temporal resolution. This section describes changes in microscope setup and the principle of the temporal measurement of vortex oscillations. We see a scheme of a time-resolved Miranda in Figure 6.2.

We use two synchronized pulse generators. The first generates a triggering signal at a frequency 5 MHz. This signal triggers electric pulses of a pulse generator Avtech and also laser pulses of picosecond laser Pilas. Laser pulses are triggered after a 100 ns delay. The second signal generator generates a gating signal at a frequency 21kHz. The gating is important for a lockin method.

The electric pulsing is periodically switched on-off at gating frequency, while the laser pulsing runs continually. Electric pulses go via picoprobe to an antenna deposited on a sample. This antenna creates a local magnetic field. The beam of laser pulses is focused on the sample. Here we decentralized the beam in objective to increase the incident angle. The plane of the incidence is parallel to the magnetic field generated by the antenna, and we detect a longitudinal magnetization.

The reflected beam is split by a Wollaston prism and sent to photodiodes. Here, we use a different kind of photodetector than we used for static measurement. For pump-probe, we use just a single diode detector, i.e., 1+1 photodiodes, one for each splitted beam from Wollaston prism. We choose this more simple solution to increase a signal-to-noise ratio. A half-wave plate (HWP) is used to align the same average intensity at both photodiodes. The photodiode detector also works like a differential amplifier and outputs a differential signal of the two diodes. The differential signal is further amplified and then sent to a lockin amplifier. This lockin amplifier picks up only that part of the signal, which is caused by antenna pulses because they correspond to gating frequency. Thanks to that, we are free from random signal shifts. This cleaned signal is then read by DAQ and sent to a computer.

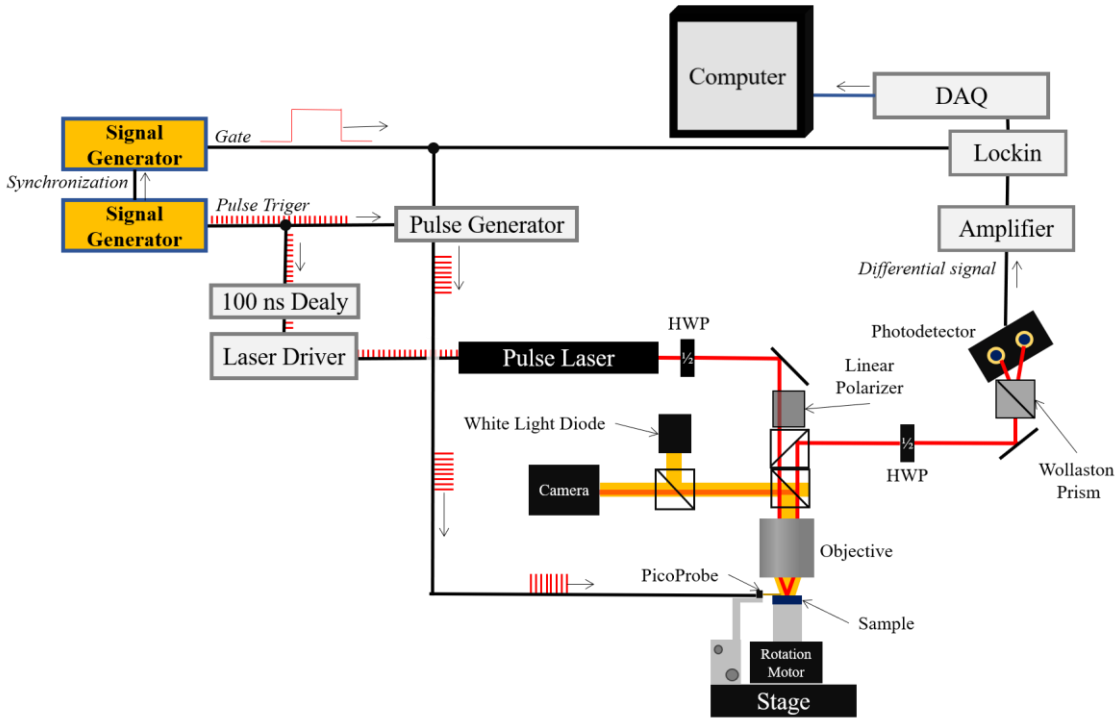

Figure 6.2 The scheme of microscope Miranda for time-resolved measurements. We use two synchronized pulse generators. The first generates a triggering signal at a frequency 5 MHz. This signal triggers electric pulses of a pulse generator Avtech and also laser pulses of picosecond laser Pilas. Laser pulses are triggered after a 100 ns delay. The second signal generator generates a gating signal at a frequency 21kHz. The gating is important for a lockin method.

The electric pulsing is periodically switched on-off at gating frequency, while the laser pulsing runs continually. Electric pulses go via picoprobe to an antenna deposited on a sample. This antenna creates a local magnetic field. The beam of laser pulses is focused on the sample under a nonzero incidence angle. The plane of the incidence is parallel to the magnetic field generated by the antenna. The reflected beam is split by a Wollaston prism and sent to photodiodes. We use a half-wave plate (HWP) to align the same average intensity at both photodiodes. The photodiode detector also works like a differential amplifier and outputs a differential signal of the two diodes. The differential signal is further amplified and then sent to a lockin amplifier. This lockin amplifier picks up only that part of the signal, which is caused by antenna pulses because they correspond to gating frequency.

The Avtech pulse generator has an internal delay, which we use to reach an artificial delay between the electric pulse and laser pulse. The electric pulses are used as a pump and laser pulses as a probe.

6.3 Sample

On our silicon sample, we have deposited an antenna[1], as we see in Figure 6.3.

[1] I am grateful to Marek Vaňatka, who prepared this sample.

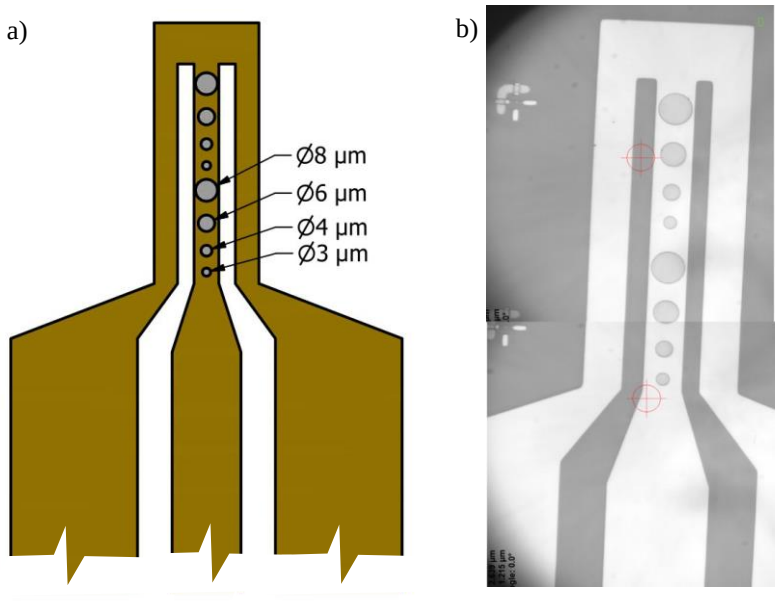

Figure 6.3 Antenna deposited on a silicon substrate. The antenna is 100nm high, made from copper, and covered by gold. Ont the top of the antenna, there are eight permalloy discs. They are 50nm high, and their diameter is 8, 6, 4, 3 µm. A Picoprobe can contact this antenna. a) Sketch. b) Photo from microscope Miranda.

The antenna is not magnetic since it is made from copper and is covered by gold. Its total height is 100 nm. There are eight permalloy discs on the top surface of this antenna with a diameter 8, 6, 4, and 3 µm. They are 50 nm high. Permalloy is a ferromagnetic and magnetically anisotropic material. Therefore, vortex structure appears in these discs in zero external field.

On the *xyz* microscope stage, we assembled a micropositioner with a Picoprobe, as we see in Figure 6.4 a).

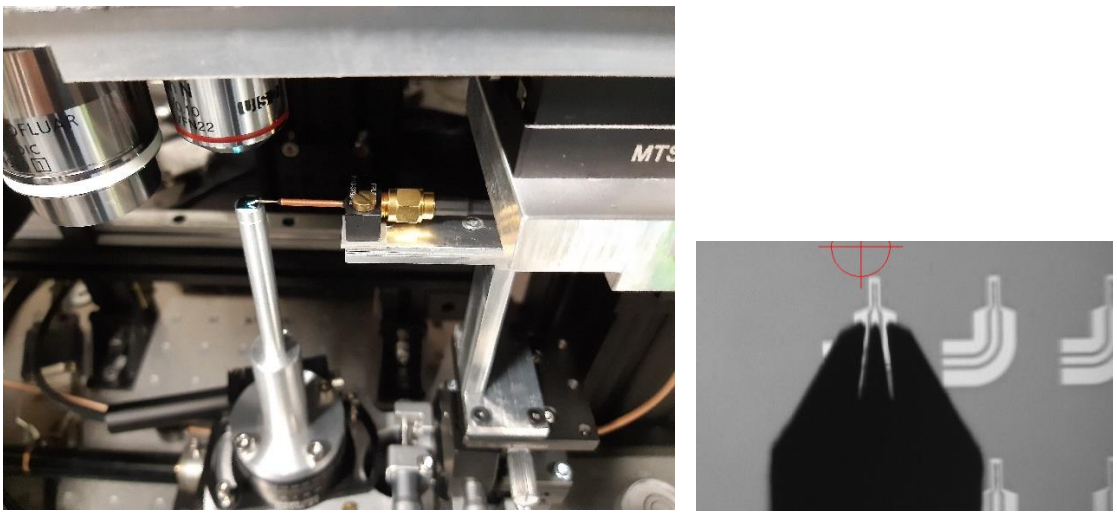

a) b)

Figure 6.4 a) Picoprobe is connecting an antenna on a sample with an external pulse generator via coaxial cable. b) The probe is landed on an antenna. We designed curved landing taps to be able to contact the antenna at any angle of rotation. This feature was not used in this experiment.

We land this Picoprobe on the antenna enlarged pads and connect the Picoprobe to the pulse generator via a coaxial cable. We see a landed probe in Figure 6.4 b).

We use the small objective with a magnification of 8x for contacting and the large with a magnification of 100x for the measurement.

We want to influence vortex magnetization by a magnetic field. Therefore, we send an electric current I through the antenna, which creates a magnetic induction $\boldsymbol{B}$ according to the following equation:

$$B = \frac{\mu_0 I}{2\pi r} \tag{6.1}$$

Here r is a distance from the current conductor. This equation (6.1) is valid for an infinitesimal thin conducting vire. Since our antenna is rectangular, we did a more precious calculation numerically by finite element method based on this equation (6.1).

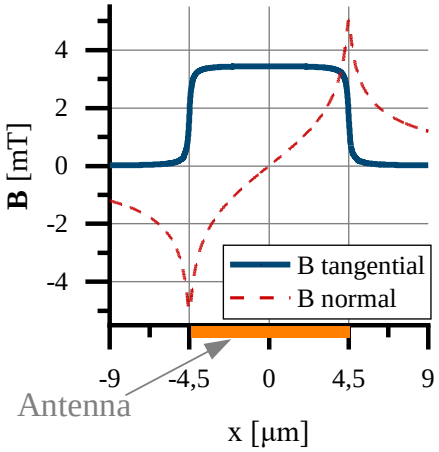

Figure 6.5 Simulation of a magnetic induction $\boldsymbol{B}$ in 50 nm above an antenna for an electric current 50 mA. The tangential component of $\boldsymbol{B}$ directs parallel to the top surface of the antenna, and the normal component of $\boldsymbol{B}$ directs perpendicularly to the top antenna surface. The simulation was done in a magnetic simulation software FEMM[1].

[1] I am greateful to Kristýna Davídková, who calculated this simulation.

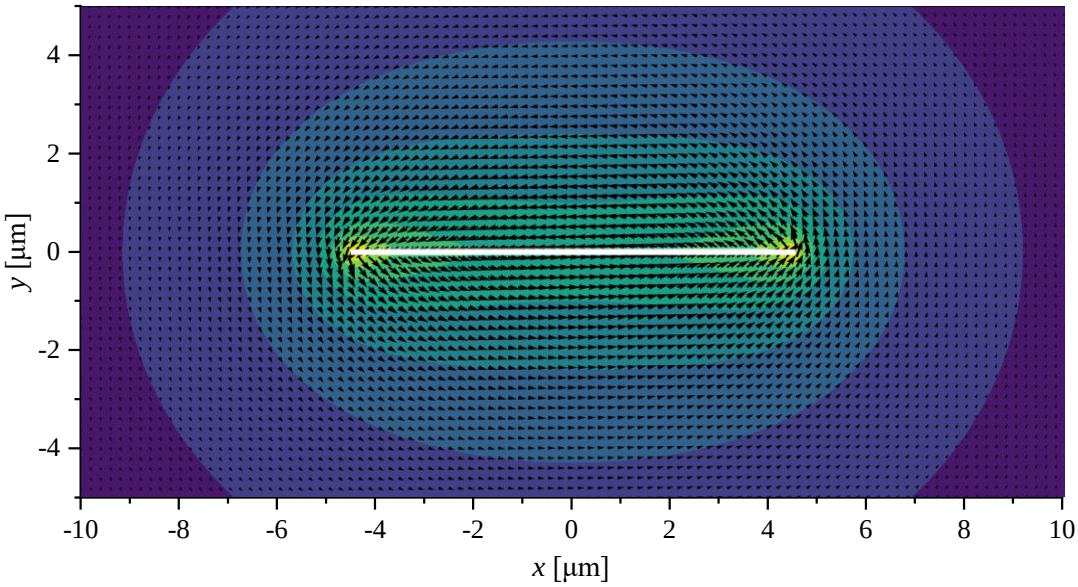

Figure 6.6 Schematic plot of a magnetic field in the antenna crossection. The antenna is colored white. This graph was calculated by the finite element method in Python.

As we see in Figure 6.5, the magnetic field $\boldsymbol{B}_{\text{tangential}}$ is homogeneous at a close distance from the antenna surface, where is placed our magnetic structure. Figure 6.6 shows the magnetic field as it drops with increasing distance from the antenna. Since we create more than 3 mT per 50 mA, the magnetic field is strong enough to manipulate the magnetization.

6.4 Measurement

Now, we want to show representative results of our measurement. We sent electric pulses from the Avtech pulse generator to the antenna. Their amplitude was 5 V (±50%), and their width was 1 ns. We measured that the resistance of our antenna is 12 Ω, so we can calculate that the corresponding amplitude of the magnetic field is approximately 25 mT. We can see the shape of the electric pulse in Figure 6.7.

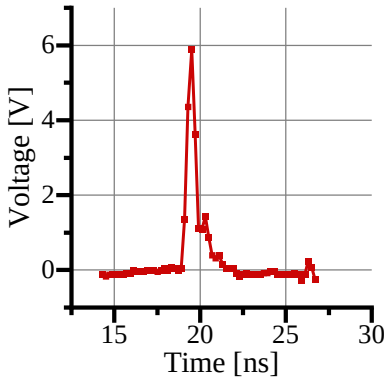

Figure 6.7 The electric pulse generated by the Avtech pulse generator. We measured this pulse by an oscilloscope. The nominal parameters of the pulse generator were 4 V amplitude and width 1ns. All pulses are not precisely the same since they vary from a nominal value ±50%.

We also focus the laser pulses to the center of a permalloy disc on the antenna. The magnetization of the structure alters the polarization of the reflected pulses by the Kerr effect. In this way, we measure the rotation of the polarization, which is proportional to the magnetization. Since we can control delay by a variable delay of the Avtech pulse generator, we measure this step by step with an increasing delay between the electric pulse and the laser pulse. Thanks to this process, we cover a whole time interval of 65 ns. The results of this measurement are in Figure 6.9.

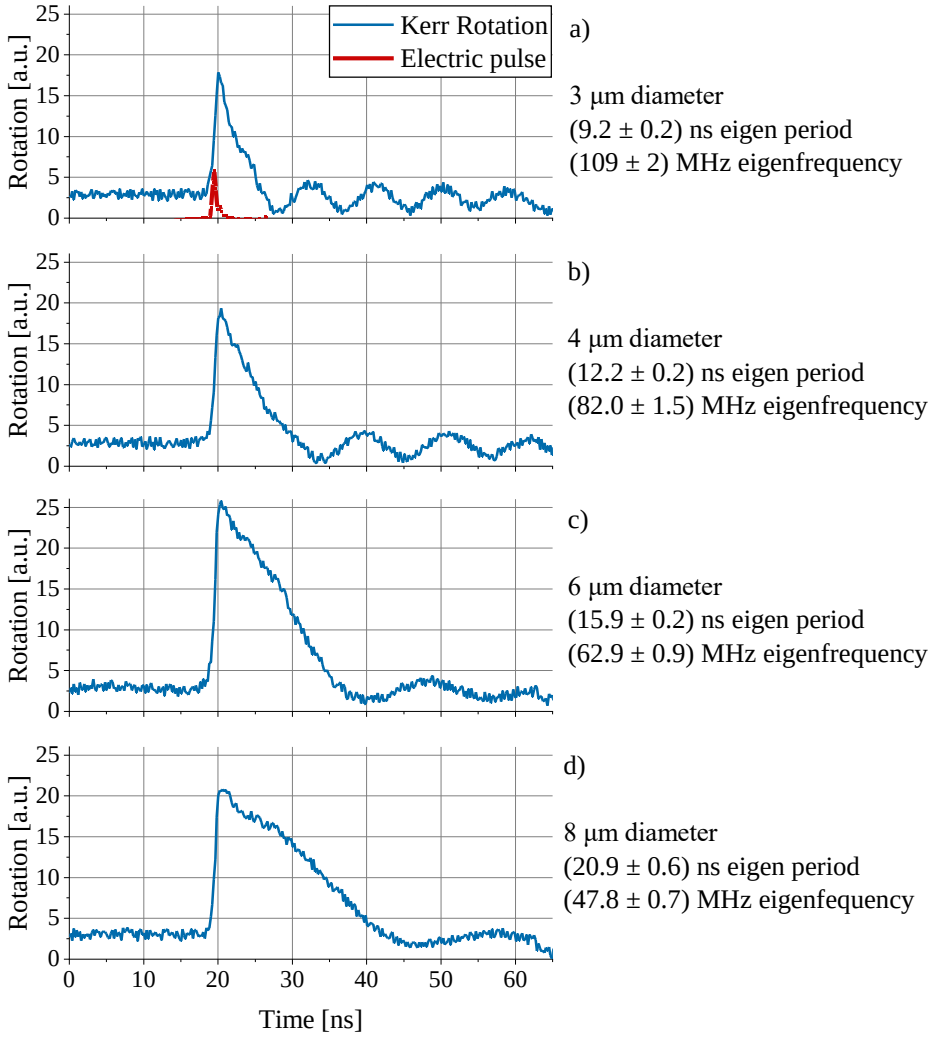

Figure 6.8 Measurement of the Kerr rotation at four permalloy discs. The measured Kerr rotation is proportional to a longitudinal magnetization. The laser spot was aligned to the central position of each disc. An electric pulse excites the magnetization and pushes the vortex core from its equilibrium position approximately in time = 19 ns. Then, the vortex core comes back and oscillates around the center of the disc at a certain eigenfrequency. The eigenfrequency depends on the disc diameter.

As we see in Figure 6.8, the magnetization is still at the beginning of the measurement. The electric pulse comes approximately in the time 18 ns. Then we observe a rapid change of the magnetization which again comes back to the equilibrium state. This relaxation process performs damping oscillations around the equilibrium position. The magnetic core rotates around the center of the permalloy disc. Therefore we measure oscillations in the rotation of the laser polarization. This data shows us the eigenfrequency of the vortexes, which depends on the diameter of the structure. We compare the measured eigenfrequencies with a theoretical model. The so-called two-vortex model is expressed by equation (6.2) [21,22].

$$f_{2\text{vortex}} = \frac{5}{9}\frac{\gamma}{2\pi}\frac{\mu_0 M_s t}{\pi R} \tag{6.2}$$

Here the γ is a gyromagnetic ratio, M_s saturation magnetization, t thickness of the disc, R the radius of the disc. We compare the two-vortex model with the measured frequencies in Figure 6.9.

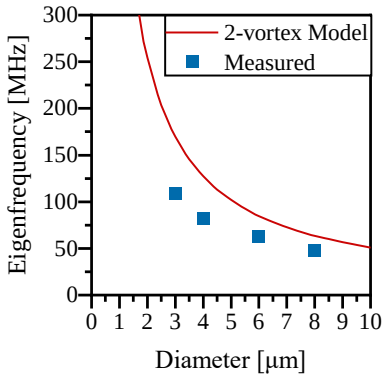

Figure 6.9 The eigenfrequency is inversely proportional to the vortex diameter.

We also measured an eigenfrequency for the various amplitude of excitation pulses. The result in Figure 6.10 shows that the eigenfrequency does not depend on the electric pulse amplitude.

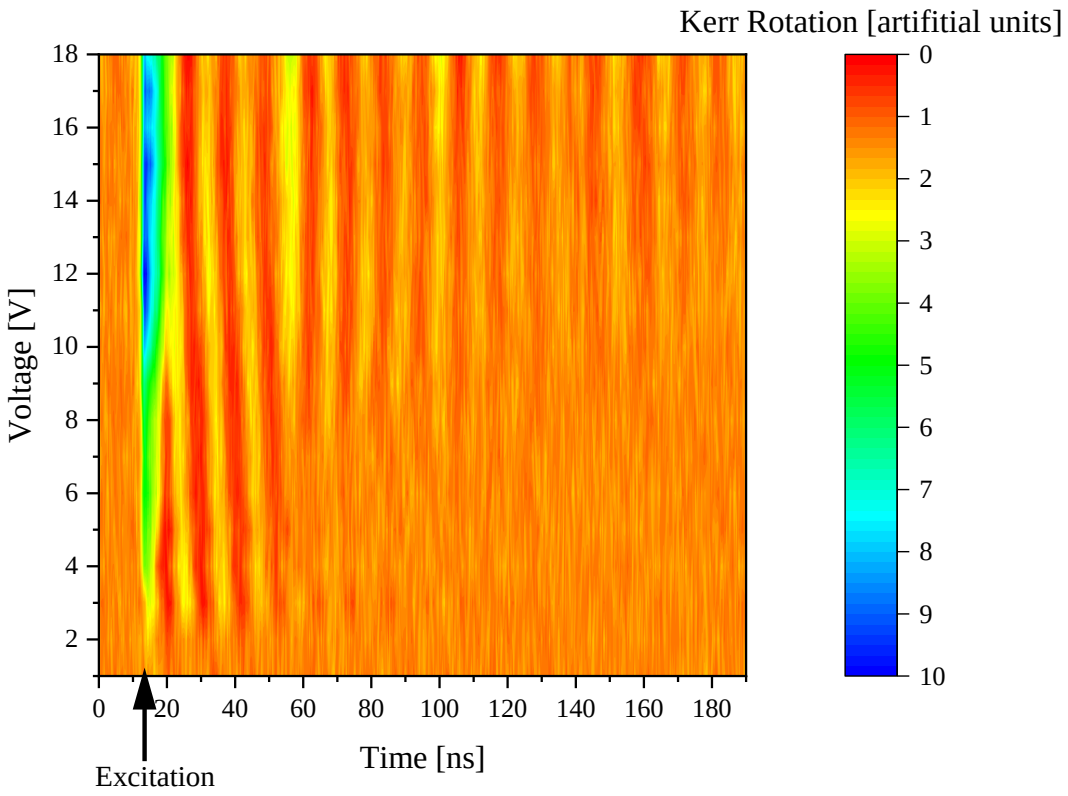

Figure 6.10 We excited a 4 μm vortex by various amplitudes of the electric pulse (vertical axis) and measured its oscillations in time. We see that the eigenfrequency does not depend on the amplitude. The higher the amplitude, the longer we can detect magnetization oscillations. The pulse length was 0.5 ns.

These vortex experiments are only the first step toward the measurements of dynamic magnetization. We proved that we are able to use the pump-probe technique and get valuable data with temporal resolution.

Conclusion

Kerr microscopy is an excellent method, how to observe the magnetization of magnetic structures. We can detect the direction of magnetization in any position on a sample or make an area scan to watch the magnetic behavior of whole structures. Kerr microscopy offers many possibilities, and our microscope Miranda makes them available in our laboratory.

In the first chapter, we introduced a theory of electromagnetic waves, polarization, and Jones formalism. This was a theoretical background for the second chapter, where we explained the magneto-optical Kerr effect. The Kerr effect is the change of light polarization by reflection on a magnetized material.

The third chapter describes optics and signal processing in our microscope. We use four-quadrant photodetectors to measure the Kerr effect along three spatial axes simultaneously. Therefore, we can detect the direction of magnetization. We also measured the spatial resolution of the laser spot. The smallest spot diameter was 0.49 μm.

The fourth chapter shows the mechanical design of the microscope.

The fifth chapter introduces a software solution and experimental results. We showed the measurement of three structures with interesting features. The last experiment demonstrated the utility of sample rotation.

The last sixth chapter deals with the time resolution. We used a pump-probe method to measure magnetic vortexes while excited and then oscillated around their equilibrium state. The measured eigenfrequencies of these oscillations are reversely proportional to the disc diameter. This fact agrees with the theoretical model. Here, we used an antenna to create a local magnetic field and excite the vortexes. Such an antenna can create high-frequency magnetic fields since the used pulse rate was 5 MHz.

We completely rebuilt the core structure of the Kerr microscope and developed the new version, Miranda 5.0. We added a new larger magnet. We also aligned optics and signal amplifiers to detect the direction of magnetization. We added a rotation motor which enables us to examine angular dependency. Microscope got new user-friendly software that allows automatic measurements. We installed a contacting picoprobe. And finally, we successfully introduced a pump-probe technique for experiments with temporal resolution.

The measurement of vortex eigenfrequencies was just a beginning where we were testing the pump-probe technique. Our next goal is to detect the propagation of spin waves with time resolution.

Bibliography

[1] A. v. Chumak, V.I. Vasyuchka, A.A. Serga, B. Hillebrands, Magnon spintronics, Nature Physics. 11 (2015). https://doi.org/10.1038/nphys3347.

[2] A. Prabhakar, D.D. Stancil, Spin waves: Theory and applications, 2009. https://doi.org/10.1007/978-0-387-77865-5.

[3] A. Mahmoud, F. Ciubotaru, F. Vanderveken, A. v. Chumak, S. Hamdioui, C. Adelmann, S. Cotofana, Introduction to spin wave computing, Journal of Applied Physics. 128 (2020). https://doi.org/10.1063/5.0019328.

[4] A. v. Chumak, A.A. Serga, B. Hillebrands, Magnon transistor for all-magnon data processing, Nature Communications. 5 (2014). https://doi.org/10.1038/ncomms5700.

[5] A. v. Chumak, Fundamentals of magnon-based computing, ArXiv. (2019).

[6] Y. Zhang, W. Zhao, J.-O. Klein, W. Kang, D. Querlioz, Y. Zhang, D. Ravelosona, C. Chappert, Spintronics for low-power computing, in: 2014. https://doi.org/10.7873/date.2014.316.

[7] J. McCord, Progress in magnetic domain observation by advanced magneto-optical microscopy, Journal of Physics D: Applied Physics. 48 (2015). https://doi.org/10.1088/0022-3727/48/33/333001.

[8] I. v. Soldatov, R. Schäfer, Advances in quantitative Kerr microscopy, Physical Review B. 95 (2017). https://doi.org/10.1103/PhysRevB.95.014426.

[9] L. Flajšman, Vectorial Kerr magnetometry, 2015.

[10] L. Flajšman, Design of the apparatus for the measurement of the magnetic properties of the micro andnanostructures, 2013.

[11] L. Flajšman, Study of dynamic properties of magnetic nanostructures and magnetic metamaterials by magneto-optical methods, 2017.

[12] D.J. Griffiths, Introduction to electrodynamics, Pearson, Boston, 1942.

[13] G. Stark, Light, Encyclopedia Britannica. (2021).

[14] Z.Q. Qiu, S.D. Bader, Surface magneto-optic Kerr effect, Review of Scientific Instruments. 71 (2000). https://doi.org/10.1063/1.1150496.

[15] A. Berger, M.R. Pufall, Generalized magneto-optical ellipsometry, Applied Physics Letters. 71 (1997). https://doi.org/10.1063/1.119669.

[16] R., C. O'Handley, Magnetic Materials, Encyclopedia of Physical Science and Technology. (2003).

[17] Understanding Waveplates and Retarders, Https://Www.Edmundoptics.Com/Knowledge-Center/Application-Notes/Optics/Understanding-Waveplates/. (2021).

[18] M.W. Davidson, M. Abramowitz, Optical microscopy-Book, Book. (2003). http://www.ncbi.nlm.nih.gov/pubmed/21685973.

[19] J. Holobrádek, Metastable iron thin films for magnetic metamaterials, 2020.

[20] G. Zhang, G. Lefkidis, M. Murakami, W. Hübner, T.F. George, Introduction to Ultrafast Phenomena from Femtosecond Magnetism to high-harmonic Generation, 2020. https://doi.org/10.1201/9780429194832.

[21] K.Y. Guslienko, B.A. Ivanov, V. Novosad, Y. Otani, H. Shima, K. Fukamichi, Eigenfrequencies of vortex state excitations in magnetic submicron-size disks, Journal of Applied Physics. 91 (2002). https://doi.org/10.1063/1.1450816.

[22] M. Vaňatka, Static and dynamic properties of nanostructured magnetic materials, 2020.

[23] J.M. Florczak, E.D. Dahlberg, Detecting two magnetization components by the magneto-optical Kerr effect, Journal of Applied Physics. 67 (1990). https://doi.org/10.1063/1.345813.

[24] R.M. Osgood, S.D. Bader, B.M. Clemens, R.L. White, H. Matsuyama, Second-order magneto-optic effects in anisotropic thin films, Journal of Magnetism and Magnetic Materials. 182 (1998). https://doi.org/10.1016/s0304-8853(97)01045-7.

[25] S. Maat, J.U. Thiele, E.E. Fullerton, Temperature and field hysteresis of the antiferromagnetic-to-ferromagnetic phase transition in epitaxial FeRh films, Physical Review B - Condensed Matter and Materials Physics. 72 (2005). https://doi.org/10.1103/PhysRevB.72.214432.

List of Abbrevitations

DAQ	Data Aquisition card
HWP	Half Wave Plate
IT	Information Technology
LED	Light Emiting Diode
NA	Numerical Aperture
QWP	Quarter Wawe Plate